Modeling the effective viscoelastic properties of PEEK matrix reinforced by arbitrary oriented short glass fibers

Boris Burgarella, Aurelien Maurel-Pantel, Noël Lahellec, Jean-Luc Bouvard, Noëlle Billon

To cite this version:

Boris Burgarella, Aurelien Maurel-Pantel, Noël Lahellec, Jean-Luc Bouvard, Noëlle Billon. Modeling the effective viscoelastic properties of PEEK matrix reinforced by arbitrary oriented short glass fibers. Mechanics of Time-Dependent Materials, 2020, 10.1007/s11043-020-09475-9 . hal-03000114

HAL Id: hal-03000114
https://hal.science/hal-03000114v1

Submitted on 11 Nov 2020

Noname manuscript No.
(will be inserted by the editor)

Modeling the effective viscoelastic properties of PEEK matrix reinforced by arbitrary oriented short glass fibers

Burgarella Boris[1] · **Maurel-Pantel Aurelien**[1] · **Lahellec Noël**[1] · **Bouvard Jean-Luc**[2] · **Billon Noëlle**[2]

Received: date / Accepted: date

Abstract The aim of this work consists to estimate and model the viscoelastic behavior at small strain of KetaSpire® KT-880 PEEK fiber composites reinforced with short glass fibers. The viscoelastic behaviour of the PEEK matrix is identified from a series of DMA tests at different temperatures. The principle of time-temperature superposition is used to build a master curve in order to identify the parameters of a generalized thirteen-branches Maxwell model. The composite's master curves are constructed by using virtual DMA experiments. These master curves are used to identify a generalized, transversely isotropic Maxwell spectral law. The modulus of each branch of the model are linked to the characteristic time of the branch by a normal distribution function (spectral law), which allows to drastically reduce the number of material parameters. Finally, a meta-model is

---

[1] Aix Marseille Univ, CNRS, Centrale Marseille, LMA, Marseille, France

[2] MINES ParisTech, CEMEF, CNRS UMR 7635, Sophia Antipolis, France

built to estimate the behavior of the composite as a function of the microstructural parameters: fiber volume fraction and fiber orientation distribution function.

Keywords Composites · Short fibers · Viscoelasticity · Full field homogenization · Dynamic Mechanical Analysis · Time-temperature equivalence · PEEK matrix

1 Introduction

Mass reduction has become one of the main goals of mechanical conceptions. Short fiber thermoplastics composites is an interesting solution since they present a good compromise between relatively easy process and mechanical properties. These characteristics explain why industries involving large volumes (like the automotive manufacturers) are increasingly interested in this kind of material. Addition of short fibers in thermoplastic resin are also used to improve the stiffness and strength of moulded parts. The materials studied in this paper are KetaSpire® KT-880 GF15 and KetaSpire® KT-880 GF30 manufactured by Solvay [1] and used in the design of the latest generation of cars. These materials are made of a polyetheretherketone (PEEK) matrix reinforced by short glass fiber (approximately 0.1 mm long and 0.01 mm in diameter) with a fiber mass ratio of 15% and 30% respectively. The PEEK matrix is a semi-crystalline thermostable thermoplastic which can be used at medium temperatures (close to its glass transition temperature, about 140 °C). To use these composite materials in mechanical parts, designers need constitutive laws to be integrated into FEA code to compute the stiffness or strength of these structures.

The objective of this work is to estimate the effective macroscopic behavior laws of such materials within the framework of linear viscoelasticity, taking into account the matrix behavior at different temperatures and the microstructure of the composite resulting from the processing (volume fraction and fiber orientation distribution).

During the past twenty years, a lot of work have been done to model the macroscopic behavior of such composite materials. All these works can be separated in two classes:

In the first one, the authors build a so-called phenomenological model by identifying the macroscopic behavior to fit some ”well chosen” experiments (see [2]). In the case of short fibers, the specimens are often obtained by injection molding and the topography of their microstructure can be obtained through micro-tomography, as can be seen in [3], [4], [5] and [6]. These micro-tomographies exhibit the complexity of the microstructure. Accounting for such complexity, information obtained from micro-tomography can be used to inform fiber orientation in macroscopic constitutive behaviors.

In the second one, the macroscopic behavior is given by homogenization methods (see for instance [7]). These methods integrate directly the effects of the microstructure parameters and the constitutive law of each constituent in the homogenized model of the composite. This can be achieved in an analytical way in the case of mean field methods (see among others [8, 9]) or given as a result of numerical simulations in the case of full field methods (see for instance [10, 11, 12]). In the case of linear viscoelasticity, by using the correspondence principle, several authors like [13] or [14] among others, find some estimates in closed form for the macroscopic laws of isotropic composites with microstructures following the Hashin Shtrikman lower bound. For more complex microstructures, the estimate given by this principle are no longer given in closed form and need numerical calculations to be

approximated (see [15] and [16] in the case of polycrystals). Another limitation of mean field methods is in the complexity of the constituents laws like the nonlinear behavior exhibited by polymer matrices (see in for the case of elastoplastic matrix [17, 18]). Full field methods can handle all this complexity but they only give the response of the composite for a particular loading path.
Following [19], we use in this work full field calculations to identify a phenomenological law presented as a meta model able to predict the composite viscoelastic macroscopic behavior depending of the volume fraction and the fiber orientation distribution.

The paper is organized as follows. The first section concerns the identification of the viscoelastic behaviour of the PEEK matrix from a series of DMA tests performed for different frequencies and temperatures. Then we use the principle of time-temperature equivalence to build a master curve. This curve is then used to identify the parameters of a generalized thirteen branches Maxwell model, the temperature dependence being taken into account by a WLF law, (see [20]). The second section concerns the identification of the macroscopic behaviour of a composite consisting of the PEEK matrix, identified in the first section, reinforced with short glass fibers with a given volume fraction and orientation distribution. Virtual DMA tests are performed using CraFT, a full-field micromechanical software. These virtual tests are used to identify a generalized, transversely isotropic spectral Maxwell law. The elastic and viscous moduli of each branch of the model are linked to the characteristic time of the branch by a normal distribution function (spectral law), which allows to drastically reduce the number of material parameters. The third and final section presents the development of a meta model. Such model allows the evolution of each of the coefficients of the spectral macroscopic law to be described as a function of the microstructural parameters (volume fraction and fiber orientation distribution function).

2 PEEK matrix characterization and modeling

In order to estimate the effective behavior of composites using homogenization techniques, one needs to know the behavior of each of its constituents. In this study, the composite is a PEEK matrix reinforced with short glass fiber (10 μm of diameter and 100 μm length). The elastic properties of the glass fibers are well known ($E_f = 70\ GPa$, $\nu = 0.3$). PEEK matrix is a semi-crystalline thermoplastic polymer. Its viscoelasticity results from the same molecular and microstructural origins as any other thermoplastic polymers. The magnitude of this latter depends on the temperature and the stress rate with a transition zone associated to the glass transition of the polymer. Thus the viscoelastic effects are less sensitive, but existing, below and above the alpha transition. The particularity of PEEK, if any, is its high glass transition temperature linked to a rigid polymer chain. In this section, the viscoelastic behavior of the PEEK matrix will be identified by using dynamic mechanical analysis experiments with temperature and frequency scans.

2.1 PEEK matrix characterization

2.1.1 Dynamic Mechanical Analysis

To characterize polymers, a common way is to use dynamic mechanical analysis. This method consists in applying sinusoidal tensile displacement to material samples, and measuring the corresponding force to compute the instantaneous modulus and the lag between strain and stress. By scanning though frequencies and/or temperature, it is possible to characterize the viscoelastic behavior of the material. For isotropic material at each temperature (or frequency), a DMA tensile test will give two independent quantities: the storage modulus which is often noted $E^{'}$ which can be linked to the stored elastic energy, the loss modulus $E^{''}$ used to quantity the energy dissipated by viscosity. These moduli are measured as follow. We applied the following tensile strain in assuming that the strain is homogeneous in the sample:

$$\varepsilon_{11}(t) = \varepsilon_0 sin(2\pi f t), \tag{1}$$

where ε_0 is the amplitude of the strain load, and f is the frequency of that load. In all the following, the frequency was transformed into an angular frequency with the usual relation $f = \frac{\omega}{2\pi}$. As a consequence of this imposed strain, comes a lagged sinusoidal stress which can be expressed through:

$$\sigma_{11}(t) = \sigma_0 sin(2\pi f t + \phi), \tag{2}$$

where the stress amplitude σ_0 and the phase lag ϕ are measured. For each frequency, E' and E'' respectively, are defined by:

$$E' = \frac{\sigma_0}{\varepsilon_0} cos\phi, \quad E'' = \frac{\sigma_0}{\varepsilon_0} sin\phi \quad \text{and} \quad tan(\delta) = \frac{E''}{E'}. \tag{3}$$

With the expression of the global complex modulus E^{**} defined by:

$$E^{**}(2\pi f) = E'(2\pi f) + iE''(2\pi f) \tag{4}$$

2.1.2 Test protocol

Previously performed DSC investigations was used to determine that the glass transition temperature (T_α) was around 160^oC and the melting temperature was around 341.5^oC. DMA tensile tests were performed between 25^oC and 200^oC to observe the evolution of the behavior around the glass transition and to avoid melting of the sample in the DMA device.

2.1.3 Temperature scans

The resin was submitted to temperature scans ranging from 25^oC to 200^oC at two different frequencies, 1 Hz and 10 Hz. Fig 1 shows the evolution (filtered curves) of $E^{'}$ and $tan(\phi)$ as a function of the temperature for 1 Hz and 10 Hz. The curves exhibit a glass transition temperature, located at 160^oC. We observed that this transition (T_g) obtained from the DMA measurement was similar to the one obtained from DSC analysis. We can also notice that the transition temperatures are shifting with the loading frequency, as higher frequencies will constrain chain motion thus increasing the glass transition temperature.

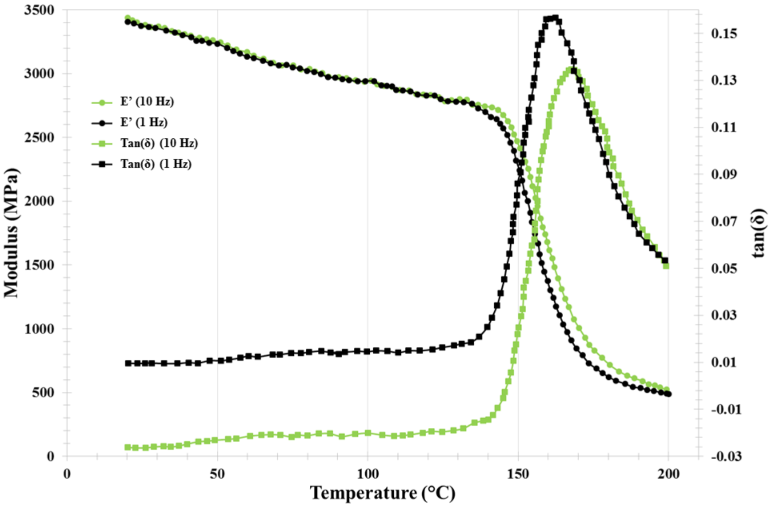

Fig. 1 Temperature scans performed on the pure PEEK matrix. The left axis is the storage modulus (MPa) and the right axis is $\tan \delta$.

2.1.4 Frequency scans and TTS principle

Unfortunately, obtaining a large range of frequencies is impossible with our experimental devices. Then, we use the Time Temperature Superposition (TTS)

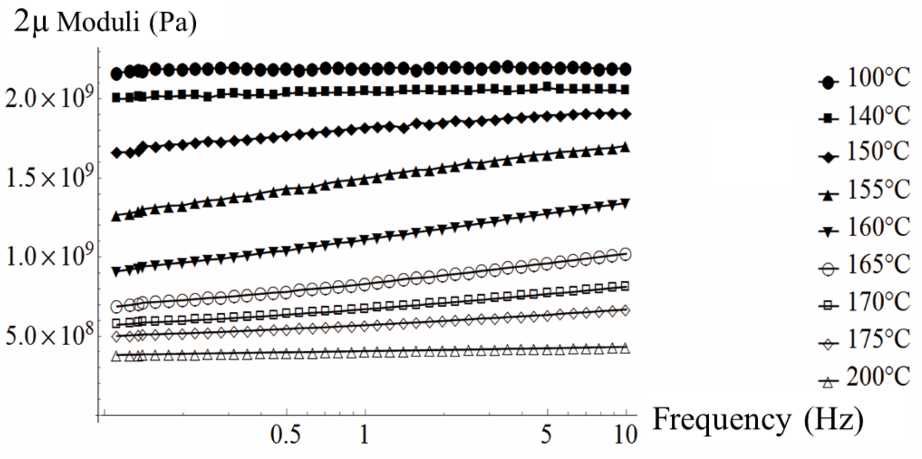

Fig. 2 Raw data of frequency scan performed from 1 to $10Hz$, and for temperatures ranging from 100^oC to 200^oC.

method (see [21, 22]) to reconstruct a large frequency scan. The TTS method uses the equation (5) (see [23]) to build the master curve of the material that account for both the effect of time and temperature on the mechanical behaviour. Therefore, we can express the storage and loss moduli as a function of an equivalent frequency f^* calculated with the so called WLF equation:

$$f^* = a_T \times f = 10^{\left(\frac{-C_1(T-T_{ref})}{C_2+(T-T_{ref})}\right)} \times f \tag{5}$$

where C_1 and C_2 are two constants to be identified and T_{ref} the reference temperature which is generally chosen close to T_α value. The matrix master curve is obtained through several DMA frequency scans (ranging from 100 to 200^{o}C and from 0.1 Hz to 10 Hz). The results of all these experiments are displayed in Fig.2[1]. The data of these frequency scans were then shifted using the a_T variables. It is possible to shift the curves and reconstruct the full master curve, as shown in Fig.3.

---

[1] In all the following the matrix master curve are plotted for the shear modulus assuming that the Poisson's ration is fully real constant $\nu = 0.37$ with the classical formula $2\mu^{**} = \frac{E^{**}}{(1+\nu)}$.

The PEEK matrix master curve is then shifted at the reference temperature $T_{ref} = 160°C$. Fig.4 and Fig.5 displays respectively the experimental PEEK matrix master curve and the a_T values identified at each temperature. The master

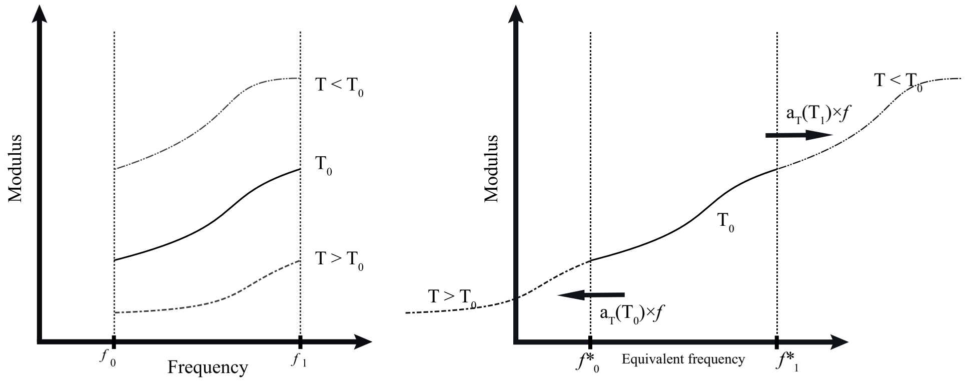

Fig. 3 TTS method illustrated, on the left are displayed the result of a temperature scan DMA, on the right are the a_T shifted results which then constitutes the master curve

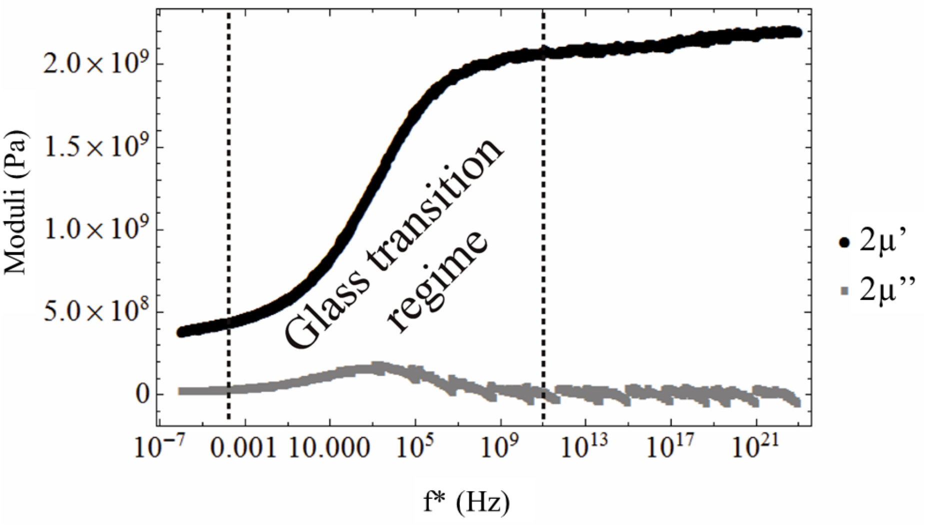

Fig. 4 Master curve built from raw data related in Fig.2. .

curve shows a decrease in the storage modulus starting at 10^9 Hz characterizing the beginning of the glass transition regime. At a frequency below 10^{-4} Hz, we start to observe the beginning of the rubbery plateau.The loss modulus curve starts to increase at the beginning of the transition regime and stabilizes back near zero. Fig.5 displays the comparison between the experimental shift and a_T obtained from the WLF equation using equation 5. The TTS principle seems to be a good approximation for the behavior of the resin using values $C1 = 35$, $C2 = 180^oC$ and $T_{ref} = 160^oC$.

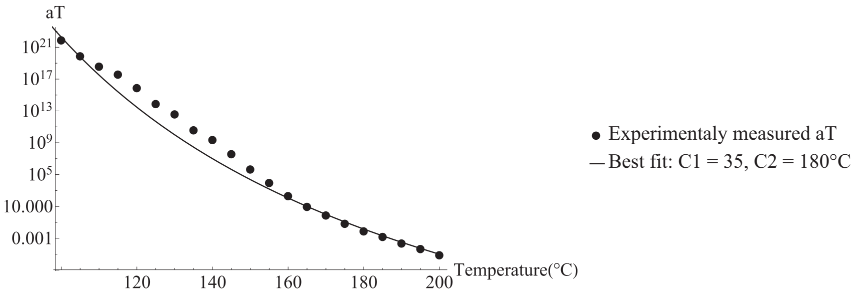

Fig. 5 Comparison between the best fit of equation 5 and the experimentally measured shift factor a_T .

2.2 PEEK matrix modeling

Therefore, the matrix will be modeled as a generalized Maxwell model (see for instance [24]) containing R viscoelastic, Maxwell-type branches for the deviatoric part of the stress and one branch characterizing the spherical part which is assumed to be perfectly elastic. The behavior law for this $(R+1)^{th}$ branch can be written as:

$$\mathrm{tr}(\boldsymbol{\sigma}^{R+1}) = \mathrm{tr}(\boldsymbol{\sigma}) = 3k\ \mathrm{tr}(\boldsymbol{\varepsilon}) \tag{6}$$

in which $\mathrm{tr}(\boldsymbol{a})$ is the trace of a 2^{nd} order tensor a, and k the bulk modulus of the material. The R first branches characterize the deviatoric behavior and for each branch j, the stress-strain relation can be given by:

$$\dot{\varepsilon}^{d} = \frac{\dot{\sigma}^{d,j}}{2\mu^{j}} + \frac{\sigma^{d,j}}{2\eta^{j}}, \tag{7}$$

in which μ^j and η^j denote the shear and viscous moduli, respectively. All these material parameters are identified to fit the master curve obtained previously and related to Fig.4. To find the complex moduli, a common way is to transform equation (7) using the laplace-Carson transform given by:

$$\hat{f}(p) = \int_{0}^{+\infty} e^{-pt} f(t)dt, \quad \text{for a time dependent function f(t)} \tag{8}$$

with $\hat{\hat{f}}(p) = p\hat{f}(p)$.

Then equation (7) becomes:

$$p\hat{\varepsilon}^{d}(p) = \frac{p\hat{\sigma}^{d,j}(p)}{\mu^{j}} + \frac{\hat{\sigma}^{d,j}(p)}{2\eta^{j}} = \frac{p\eta^{j} + \mu^{j}}{2\eta^{j}\mu^{j}}\hat{\sigma}^{d,j}(p) \tag{9}$$

Then in Laplace domain, previous equation can be given as a visco-elastic shear modulus $\hat{\mu}^{j}_{ve}$ and takes the form:

$$\hat{\sigma}^{d,j} = 2\hat{\mu}^{j}_{ve}(p)\hat{\varepsilon}^{d} \tag{10}$$

with

$$\hat{\mu}^j_{ve}(p) = \frac{\mu^j p}{p + \frac{\mu^j}{\eta^j}} \tag{11}$$

By combining (11) and (6) and expressing the combination with linear combinations of $\mathbf{K}$ and $\mathbf{J}$[2], one can obtain the expression of the constitutive law as:

$$\begin{gathered} \hat{\sigma} = \hat{\boldsymbol{L}}_{ve}(p) : \hat{\varepsilon} \\ \text{with} \quad \hat{\boldsymbol{L}}_{ve}(p) = 2\ \hat{\mu}_{ve}(p)\boldsymbol{K} + 3k\boldsymbol{J} \text{ and } \quad \hat{\mu}_{ve}(p) = \sum_{j=1}^{R} \hat{\mu}^j_{ve}(p) \end{gathered} \tag{12}$$

The determination of R (number of parallel branches to model the matrix) relies on an equilibrium between calculation time and accuracy. Different configurations were tested, and it was finally found that manually fitting $R = 12$ parallel branches to model the PEEK behavior is a good compromise. The complex tensor moduli of the master curve is given by:

$$\boldsymbol{L}^{**}_{ve}(2\pi f^*) = \hat{\boldsymbol{L}}_{ve}(i2\pi f^*), \tag{13}$$

which give the storage and loss moduli which are respectively the real and imaginary part of the complex shear modulus $\mu^{**}_{ve}(2\pi f^*)$ defined by:

$$\mu^{**}_{ve}(2\pi f^*) = \mu^{'}_{ve}(2\pi f^*) + i\mu^{''}_{ve}(2\pi f^*) \tag{14}$$

Both shear moduli $\mu^{'}_{ve}$ and $\mu^{''}_{ve}$ allowed to build the master curves of the generalized Maxwell model identified. The parameters of the proposed Maxwell model are reported in A. Fig. 6 shows the thirteen-branches model superposed to the PEEK master curve obtained experimentally. The model seems to capture the PEEK behavior quite well, except for the high frequencies, where the stored modulus continues to grow while the loss modulus gets down to zero. As described by the

---

[2] $\mathbf{K}$ and $\mathbf{J}$ are the projectors on the deviatoric and purely spheric, respectively, second order tensors spaces (i.e. $\boldsymbol{\sigma}^d = \boldsymbol{K} : \boldsymbol{\sigma}$ and $\frac{1}{3}\mathrm{tr}(\sigma)\boldsymbol{I_d} = \boldsymbol{J} : \boldsymbol{\sigma}$)

model, when $f^* \to \infty$, $\frac{d\mu'_{ve}}{df^*} \to 0$. Therefore, it is not possible to capture correctly these experiments at high frequencies.

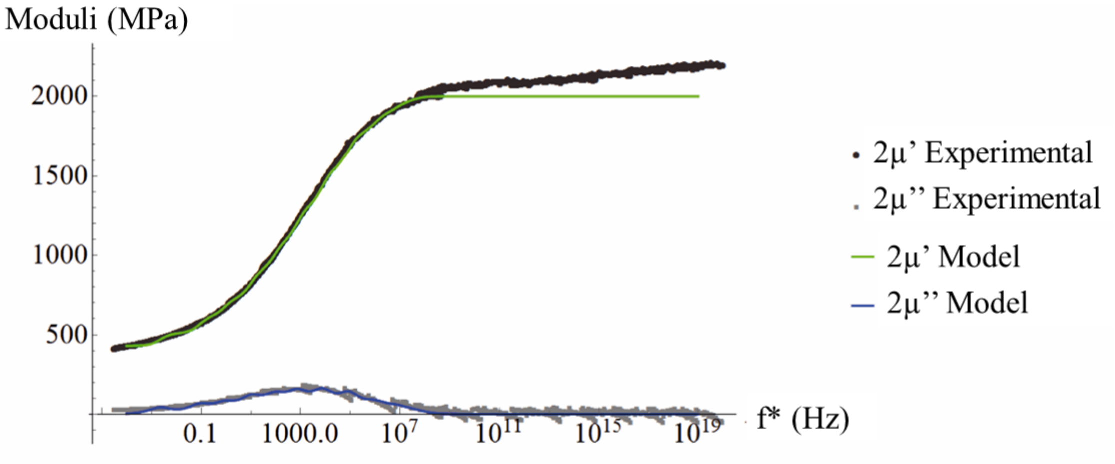

Fig. 6 Thirteen-branches Maxwell model fitted over the experimental PEEK master curve.

This behavior law is then implemented in CraFT, an homogenization software based on fast fourier transforms developped at the LMA (see [11] and [10]). Contrary to the mean field homogenization methods, this code solves exactly (up to the numerical errors) the boundary value problem. From this, we get the estimation of the RVE response when subjected to a given loading path (either a macroscopic stress or strain). The implementation was performed as follows:

For a given strain history $\varepsilon(t)$, the stress $\sigma(t)$ is the sum of the stress $\sigma^j(t)$ in each of the individual branch :

$$\sigma(t) = \sum_{j=0}^{R} \sigma^j(t) \tag{15}$$

The whole loading time is split in N time steps, For each time step t_{n+1}, the stress in each of the R first branches is calculated by using an Euler scheme which gives:

$$\dot{\sigma}_{n+1}^{d,j} = \frac{2\eta^j \mu^j \Delta t}{\eta^j + \mu^j \Delta t} \frac{\dot{\varepsilon}_{n+1}^{d,j} - \dot{\varepsilon}_{n}^{d,j}}{\Delta t} + \frac{\eta^j}{\eta^j + \mu^j \Delta t} \dot{\sigma}_{n}^{d,j}, \tag{16}$$

with $\dot{\varepsilon}_{n+1}^{d,j}$ given and $\dot{\varepsilon}_{n}^{d,j}$ and $\dot{\sigma}_{n}^{d,j}$ stored from the previous time step. This new implementation has then been tested to make sure that no errors were made in the implementation process. To do so, virtual DMA were computed following the methodology described in our previous paper (see [19]) and described in section 3.3. The CraFT (FFT) modeling of a pure matrix sample DMA superimposed to the model results is displayed in Fig. 7.

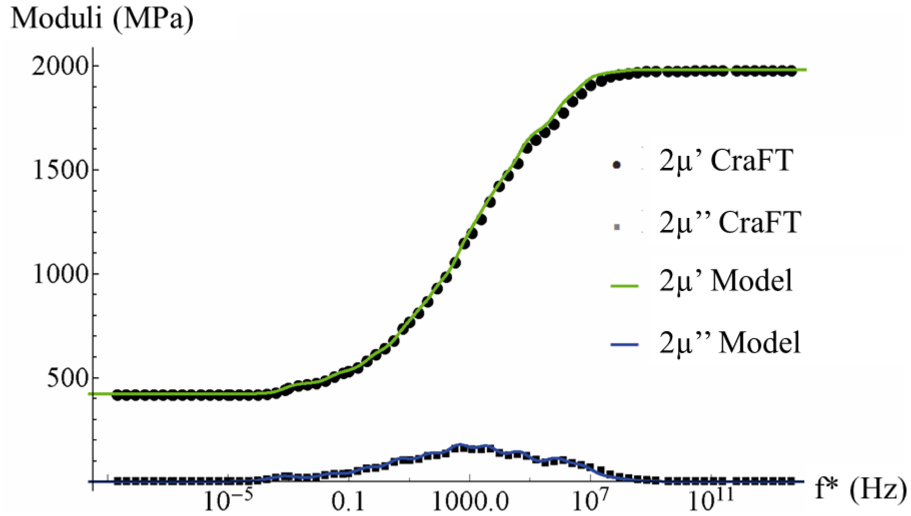

Fig. 7 Validation in CraFT of the generalized Maxwell model implementation.

3 Composite effective behavior

The final objective of the paper is to find a meta-model which gives a good estimate for the effective viscoelastic behavior of the composite, taking into account the fibers volume fraction and the fibers orientation distribution. This means that the material parameters of the composite law will be function of these fibers properties (ratio and orientation distribution).

As can be seen in the previous section, the behavior of this composite's PEEK matrix can be modeled by a generalized Maxwell model involving 26 parameters (containing 12 different relaxation times). It is now well known that the viscoelastic behavior of such a composite (reinforced matrix type) must include at least as much relaxation time as the one of its matrix. In [14] it is shown that the viscoelastic behavior of an isotropic composite, constituted of an isotropic viscoelastic Maxwell matrix with one relaxation time, involve 3 different relaxation times. Assuming that the fibers distribution induces a transversely isotropic overall behavior, the composite constitutive equation should include at least 77 material parameters (6 for the elastic branch and 5 for each of the viscoelastic one as will be seen in section 3.2). An attempt to fit the evolution of each of these variables with respect to the microstructural properties has been done, but none of the known global optimization algorithm gave satisfactory solutions. This can be explained by the very large number of parameters to be identified and because the underlying mathematical problem is known to be ill-posed, as can be seen in [25]. So the methodology that we proposed in [19] is not an option anymore, and to reduce the number of parameters in the composite law, a spectral generalized Maxwell model has been developed, inspired by previous works available in the literature [26, 27].

3.1 Spectral Maxwell model: scalar expression

The first step, in the adaptation of [26, 27] for the present case is to find the scalar expression of such a model applied for Maxwell branches. We recall the expression in the Laplace space of the generalized Maxwell model for the single modulus $\hat{\mu}_{ve}(p)$ as given in equation (12) :

$$\begin{array}{c} \hat{\mu}_{ve}(p) = \sum_{j=1}^{R+1} \frac{\mu^j p}{p+2\pi f^j} \\ \text{with} \quad 2\pi f^j = \omega^j = \frac{1}{\tau^j} = \frac{\mu^j}{\eta^j} \end{array} \tag{17}$$

with f^j, ω^j, τ^j, respectively the characteristic frequency, the characteristic angular frequency, and the characteristic relaxation time of the j^{th} branch. In this spectral model, each moduli μ^j is linked to the characteristic frequency f^j thanks to a distribution function. It is therefore possible to have any number of relaxation times, depending on the refinement needed to fit the master curve. With these methodology different distribution functions can be used as in Courtois et al. [28]. We propose in this paper, as in Vieille et al. [26] and Albouy et al. [27], to use a Gaussian distribution, which give the following expression for μ^j:

$$\begin{cases} m^j = g(log(f^j)|\Gamma, M) = \frac{1}{\Gamma\sqrt{2\pi}} e^{\dfrac{-(\log f^j - M)^2}{2\Gamma^2}}, \\ \bar{m}^j = \dfrac{m^j}{\sum_{j=1}^{R+1} m^j}, \\ \mu^j(\Gamma, M, f^j) = \mu_{ve,0} \times \bar{m}^j, \end{cases} \tag{18}$$

where M and Γ are respectively the mean and standard deviation of the normal distribution of $log(f)$. Usually, generalized Maxwell models are defined with a set of R branches (defined by their stiffness μ^j and their viscosity η^j). Here, we defined an odd number of R+1 branches with $R = 2n$. The stiffness modulus $\mu_{ve,0}$ characterizes the short time response of the material. Finally, we have R+1 pairs of

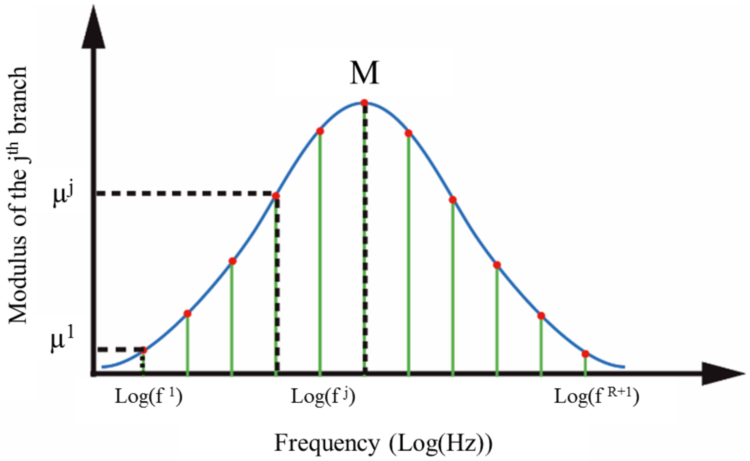

Fig. 8 Scheme of the procedure to determine the modulus of the j^{th} branch μ^j .

(μ^j,f^j), and these pairs are regularly distributed (on a logarithmic scale) around M. The contributions of each branch can be symmetrically distributed around this characteristic angular frequency noted M and the μ^j are directly obtained as related in Fig.8. The frequencies f^j are chosen around M between $10^{M-6\Gamma}$ and $10^{M+6\Gamma}$ and can be expressed with:

$$f^j(M,\Gamma) = 10^{M+6\Gamma(\frac{2(j-1)}{R}-1)} \tag{19}$$

Similarly to what is presented in the matrix modelling section, to simplify the identification procedure, the spectral model is expressed in the Laplace-Carson space as expressed in equations (12). Taking into account equations (17), (19) and (18), the scalar spectral generalized maxwell model depends on 4 variables $\mu_{ve,0}$, M, Γ and R as:

$$\hat{\mu}_{ve}(p) = \sum_{j=1}^{R+1} \frac{\mu^j(\Gamma,M,f^j(\Gamma,M))\,p}{p+2\pi f^j(\Gamma,M)} = \sum_{j=1}^{R+1} \frac{\bar{m}^j(\Gamma,M,f^j(\Gamma,M))\mu_{ve,0}\,p}{p+2\pi f^j(\Gamma,M)}, \tag{20}$$

Different cases were tested to see the effect of distribution parameters M and Γ on generalized Maxwell model master curves for $\mu_{ve}^{'}$ and $\mu_{ve}^{''}$. These effects

ID	Γ (log(Hz))	M log(Hz)
1	20	log(100)
2	10	log(100)
3	5	log(100)
4	20	log(10^7)

Table 1 Definition of the different distributions displayed in Fig.9 and Fig.10.

can be seen in Fig.9 and in Fig.10. The values of Γ and M used for the four distributions are reported in table 1. Diminishing Γ widens the distribution, and therefore makes the μ'_{ve} transition less progressive. It also increases the maximum value of the μ''_{ve} dissipation peak. The M parameter centers the μ'_{ve} transition and the μ''_{ve} dissipation peak.

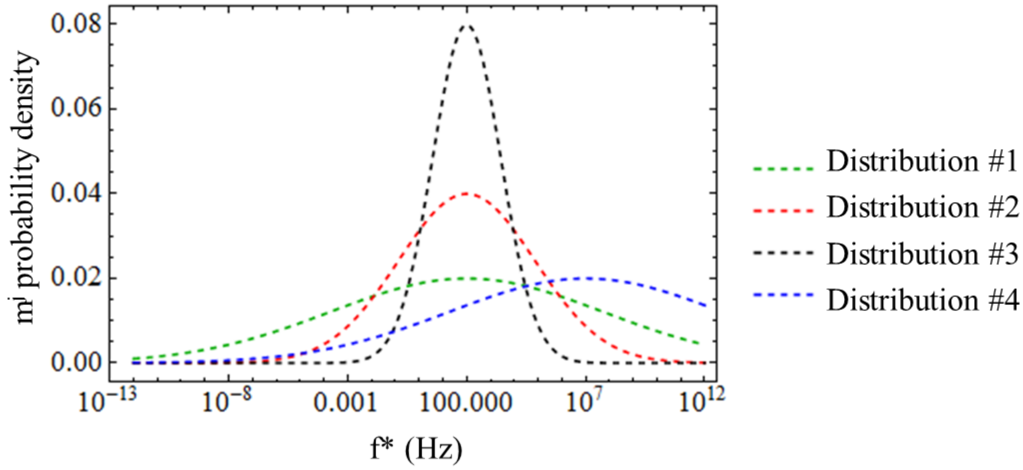

Fig. 9 Effect of M and Γ on the distribution. The parameters of each distribution are defined in Table 1.

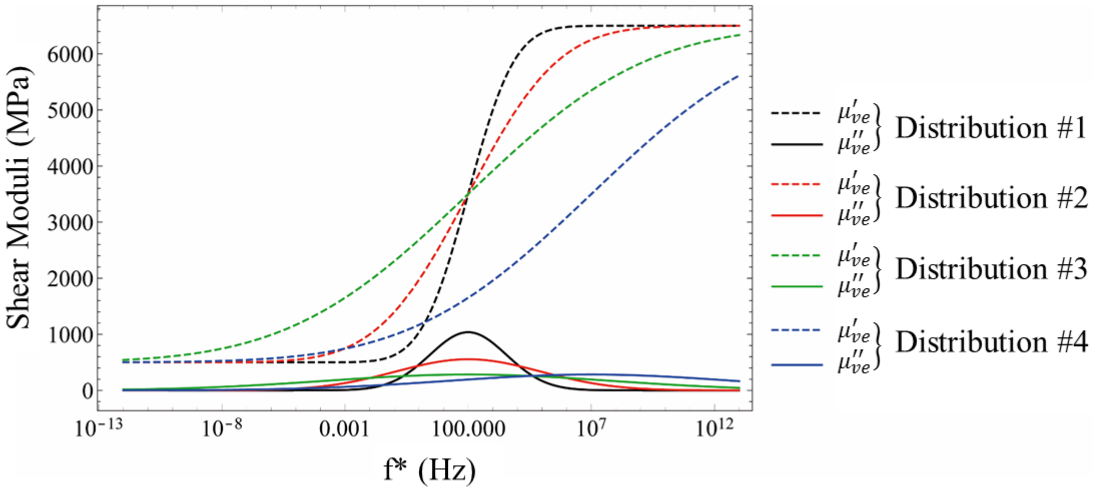

Fig. 10 Effect of M and Γ on generalized spectral Maxwell model master curves for $\mu_{ve}^{'}$ and $\mu_{ve}^{''}$.

3.2 3D Expression

So far, the spectral model has only been expressed in one dimension. Yet, this study is devoted to the behavior of transversely isotropic composite materials. In the Laplace Carson space, the viscoelastic behavior of the composite can be defined by $\hat{\boldsymbol{L}}_{ve}(p)$ which is the tensor of viscoelastic moduli:

$$\hat{\sigma} = \hat{\boldsymbol{L}}_{ve}(p) : \hat{\varepsilon} \tag{21}$$

Assuming that this behavior can be modeled by a generalized Maxwell model containing one elastic branch and $R+1$ viscoelastic branches, $\hat{\boldsymbol{L}}_{ve}(p)$ can be written as

$$\hat{\boldsymbol{L}}_{ve}(p) = \hat{\boldsymbol{L}}^{V}_{ve}(p) + \hat{\boldsymbol{L}}^{E}_{ve}(p) \tag{22}$$

where $\hat{\boldsymbol{L}}^{E}_{ve}(p)$ describes the elastic part of the behaviour and $\hat{\boldsymbol{L}}^{V}_{ve}(p)$ describes the viscoelastic part.

3.2.1 Elastic part

As can be seen in B, assuming that the overall behavior of the composite is transversely isotropic, the tensor $\hat{\boldsymbol{L}}^{E}_{ve}(p)$ can be written with the five independent parameters α_0, β_0, λ_0, δ_0, and γ_0 as :

$$\hat{\boldsymbol{L}}^{E}_{ve}(p) = \alpha_0 \boldsymbol{E}_L + \beta_0 \boldsymbol{J}_T + \lambda_0(\boldsymbol{F} + \boldsymbol{F}^T) + \delta_0 \boldsymbol{K}_T + \gamma_0 \boldsymbol{K}_L, \tag{23}$$

3.2.2 Visco-elastic part

In addition of being transversely isotropic, we assume that the dissipation in the composite can only occur for macroscopic loading involving shear. This is true for the matrix behavior, as shown by the constitutive law expressed in equation (12).

However, it might not be the case for the composite behavior because a purely spherical loading (i.e $\varepsilon \ / \ tr(\varepsilon) \neq 0$) involves local shear strain within the matrix which implies dissipation. Yet, this hypothesis simplifies the proposed macroscopic model. As it will be shown in the results of section 4.2, the dissipation remains relatively low in the case of pure spherical loading for the studied composite. As can be seen in B, $\hat{\boldsymbol{L}}^{V}_{ve}(p)$ can be written:

$$\hat{\boldsymbol{L}}^{V}_{ve}(p) = \frac{3}{2}\hat{\alpha}_{ve}(p)\boldsymbol{K}_E + \hat{\delta}_{ve}(p)\boldsymbol{K}_T + \hat{\gamma}_{ve}(p)\boldsymbol{K}_L \tag{24}$$

In expression (24), α_{ve}, δ_{ve}, and γ_{ve} denote the 3 moduli in the 3 orthogonal directions. Each of them are given by the spectral law equation (20) as:

$$\begin{aligned}
\hat{\alpha}_{ve}(p) &= \sum_{j=1}^{R+1} \frac{\bar{m}^j_\alpha \ \alpha_{ve,0} \ p}{p + 2\pi f^j_\alpha}, \quad \text{with} \quad \bar{m}^j_\alpha = \bar{m}^j(\mathit{\Gamma}_\alpha, M_\alpha, f^j_\alpha), \quad f^j_\alpha = 10^{M_\alpha + 6\mathit{\Gamma}_\alpha(\frac{2(j-1)}{R}-1)} \\
\hat{\delta}_{ve}(p) &= \sum_{j=1}^{R+1} \frac{\bar{m}^j_\delta \ \delta_{ve,0} \ p}{p + 2\pi f^j_\delta}, \quad \text{with} \quad \bar{m}^j_\delta = \bar{m}^j(\mathit{\Gamma}_\delta, M_\delta, f^j_\delta), \quad f^j_\delta = 10^{M_\delta + 6\mathit{\Gamma}_\delta(\frac{2(j-1)}{R}-1)}, \\
\hat{\gamma}_{ve}(p) &= \sum_{j=1}^{R+1} \frac{\bar{m}^j_\gamma \ \gamma_{ve,0} \ p}{p + 2\pi f^j_\gamma}, \quad \text{with} \quad \bar{m}^j_\gamma = \bar{m}^j(\mathit{\Gamma}_\gamma, M_\gamma, f^j_\gamma), \quad f^j_\gamma = 10^{M_\gamma + 6\mathit{\Gamma}_\gamma(\frac{2(j-1)}{R}-1)}
\end{aligned} \tag{25}$$

Note that we choose to take the same number of branches in each direction.

3.2.3 Global 3D spectral model expression of the composite

In the Laplace domain, the effective behavior of the composite is defined by[3]:

$$\hat{\boldsymbol{\Sigma}} = \left(\hat{\boldsymbol{L}}^{E}_{ve}(p) + \hat{\boldsymbol{L}}^{V}_{ve}(p)\right) : \hat{\boldsymbol{E}} = \hat{\boldsymbol{L}}_{ve}(p) : \hat{\boldsymbol{E}} \tag{26}$$

---

[3] we choose, in order to avoid to be confused with the matrix behavior law formalism in equation (12), to note stress and strain with capital letters (respectively $\boldsymbol{\Sigma}$ and $\boldsymbol{E}$) which are the average stress and strain of the composite RVE.

with

$$\hat{\boldsymbol{L}}_{ve}(p) = (\alpha_0+\hat{\alpha}_{ve})\boldsymbol{E}_L+(\beta_0+\frac{\hat{\alpha}_{ve}}{2})\boldsymbol{J}_T+(\lambda_0-\frac{\sqrt{2}}{2}\hat{\alpha}_{ve})(\boldsymbol{F}+\boldsymbol{F}^T)+(\delta_0+\hat{\delta}_{ve})\boldsymbol{K}_T+(\gamma_0+\hat{\gamma}_{ve})\boldsymbol{K}_L \tag{27}$$

As what we did for the matrix law in equation (13), we define the complex tensor moduli by:

$$\boldsymbol{L}_{ve}^{V**}(2\pi f^*) = \hat{\boldsymbol{L}}_{ve}^{V}(i2\pi f^*) \tag{28}$$

which give for each direction the storage and loss moduli which are respectively the real and imaginary part of each complex moduli $\alpha_{ve}^{**}(2\pi f^*)$, $\delta_{ve}^{**}(2\pi f^*)$ and $\gamma_{ve}^{**}(2\pi f^*)$ defined by:

$$\begin{aligned}
\alpha_{ve}^{**}(2\pi f^*) &= \alpha_{ve}^{'}(2\pi f^*) + i\alpha_{ve}^{''}(2\pi f^*) = \sum_{j=1}^{R+1} \frac{\bar{m}_{\alpha}^{j}\ \alpha_{ve,0}\ if^*}{if^* + f_{\alpha}^{j}} \\
\delta_{ve}^{**}(2\pi f^*) &= \delta_{ve}^{'}(2\pi f^*) + i\delta_{ve}^{''}(2\pi f^*) = \sum_{j=1}^{R+1} \frac{\bar{m}_{\delta}^{j}\ \delta_{ve,0}\ if^*}{if^* + f_{\delta}^{j}} \\
\gamma_{ve}^{**}(2\pi f^*) &= \gamma_{ve}^{'}(2\pi f^*) + i\gamma_{ve}^{''}(2\pi f^*) = \sum_{j=1}^{R+1} \frac{\bar{m}_{\gamma}^{j}\ \gamma_{ve,0}\ if^*}{if^* + f_{\gamma}^{j}}
\end{aligned} \tag{29}$$

with f^* the equivalent frequency given by the WLF relation related in equation (5).

3.3 Virtual DMA experiments: full field micromechanical computation

The 14 parameters required to make the full 3D model, (α_0, β_0, λ_0, δ_0, γ_0, $\alpha_{ve,0}$, $\delta_{ve,0}$, $\gamma_{ve,0}$, M_α, M_δ, M_γ, $\varGamma_\alpha$, $\varGamma_\delta$ and finally $\varGamma_\gamma$) given in equations (25) and (27), are found to fit virtual DMA experiments. This virtual experiments are done with CraFT which is used to solve the homogenization problem thanks to the FFT method [29][30] on RVE (Representative Volume Element) as can be see in previous works [19].

3.3.1 $\boldsymbol{L}^{**}_{ve}$ projections

As observed in equation (27), five different transversely isotropic fourth order tensors can be expressed in a basis containing five different tensors. Five different measurements have to be done on the RVE. There is no uniqueness for these set of experiments. The only constrain is that all experiments have to be linearly independent. Thus, we choose to apply the following strain on the RVE of the composite:

$$\left\{\begin{array}{lcr} V_E & = & -\frac{1}{2}(e_3 \otimes e_3 + e_2 \otimes e_2) + e_1 \otimes e_1 \\ V_T & = & \frac{1}{2}(e_3 \otimes e_3 - e_2 \otimes e_2) + e_3 \otimes e_2 + e_2 \otimes e_3 \\ V_L & = & e_1 \otimes (e_3 + e_2) + (e_3 + e_2) \otimes e_1 \\ V_S & = & e_1 \otimes e_1 + e_3 \otimes e_3 + e_2 \otimes e_2 \\ V_{S1} & = & e_1 \otimes e_1 \\ V_{S2} & = & V_S - e_1 \otimes e_1 \end{array}\right. . \tag{30}$$

The five projections of the complex tensor moduli $\boldsymbol{L}^{**}_{ve}$, related in equation (27), for each chosen directions are given in the following expression :

$$\left\{\begin{array}{lclcc} P_{V_E} & = & \frac{(\boldsymbol{L}^{**}_{ve}:V_E):V_E}{V_E:V_E} & = & \frac{3}{2}\alpha^{**}_{ve}(2\pi f^*) + \frac{2}{3}\alpha_0 + \frac{1}{3}\beta_0 - \frac{2\sqrt{2}}{3}\lambda_0 \\ P_{V_T} & = & \frac{(\boldsymbol{L}^{**}_{ve}:V_T):V_T}{V_T:V_T} & = & \delta^{**}_{ve}(2\pi f^*) + \delta_0 \\ P_{V_L} & = & \frac{(\boldsymbol{L}^{**}_{ve}:V_L):V_L}{V_L:V_L} & = & \gamma^{**}_{ve}(2\pi f^*) + \gamma_0 \\ P_{V_{S1}} & = & \frac{(\boldsymbol{L}^{**}_{ve}:V_S):V_{S1}}{V_{S1}:V_{S1}} & = & \beta_0 + \frac{\sqrt{2}}{2}\lambda_0 \\ P_{V_{S2}} & = & \frac{(\boldsymbol{L}^{**}_{ve}:V_S):V_{S2}}{V_{S2}:V_{S2}} & = & \alpha_0 + \sqrt{2}\lambda_0 \end{array}\right. . \tag{31}$$

3.3.2 Virtual DMA computation

The easier way to do these virtual DMA experiment should be to solve the set of equation given by the homogenization problem directly in the complex domain.

Unfortunately our code (CraFT) can not achieve that. We choose to follow work from [19, 31] to compute DMA experiments in temporal space. For instance, the numerical values of the storage and loss part of the projection[4] $P_{V_E}(\boldsymbol{L}_{ve}^{**})^{ne}$ related in the equation (27), for a given characteristic frequency f, is computed in the following way:

1. The applied strain is:

$$E(t) = \varepsilon_0 V_E * sin(2\pi f t), \tag{32}$$

   with ε_0 chosen as 0.05.

2. The macroscopic stress projection $\Sigma : V_E$ is then calculated.

$$\frac{\Sigma(t) : V_E}{V_E : V_E} = \sigma_0 sin(2\pi f t + \phi(f)) = P_{V_E}(\boldsymbol{L}_{ve}^{**})^{ne} = P_{V_E}^{ne} \tag{33}$$

3. Following (3), we find the storage and loss moduli of the projection $P_{V_E}(\boldsymbol{L}_{ve}^{**})^{ne}$ by:

$$\left\{\begin{array}{llll} P_{V_E}^{'ne} = Re(P_{V_E}^{ne}) & = \frac{3}{2}\alpha_{ve}^{'}(2\pi f) + \frac{2}{3}\alpha_0 + \frac{1}{2}\beta_0 - \frac{2\sqrt{2}}{3}\lambda_0 & = \frac{3}{2}\frac{\sigma_0}{\varepsilon_0}cos(\phi(f)) \\ P_{V_E}^{''ne} = Im(P_{V_E}^{ne}) = & \frac{3}{2}\alpha_{ve}^{''}(2\pi f) & = \frac{3}{2}\frac{\sigma_0}{\varepsilon_0}sin(\phi(f)) \end{array}\right. . \tag{34}$$

For other loading directions, computations are done in the exact same way by replacing V_E by V_T, V_L, V_{S1} and V_{S2} respectively.

3.3.3 Virtual master curves

Then, to build the whole virtual master curves of the composite for each direction, we need to run frequency scans from very low to very high frequencies (10^{-5}Hz

---

[4] ^{ne} stands for Numerical Experiments

to 10^{10} Hz in the present case). This induces at high frequencies and at low frequencies a significant increase of the calculation time. To solve this problem, we choose to use the time-temperature equivalence to describe the behaviour of the composite PEEK matrix. Therefore, an emulation of the real experimental protocol has been conducted thanks to the TTS principle described in equation (5). To follow this experimental protocol, virtual DMAs were run from 100^oC to 200^oC, each time through 8 frequencies from 0.1 to 10 Hz. For each branch, the PEEK matrix Maxwell model implemented in CraFT with the temperature dependence is expressed as in [24]:

$$\dot{\varepsilon}(T) = \sum_{j=1}^{12} \left(\frac{\dot{\sigma^j}}{2\mu^j} + \frac{2\pi f^{*j}(T)\sigma^j}{2\mu^j} \right), \tag{35}$$

with T the temperature, μ^j the shear modulus, and $f^{*j}(T)$ the equivalent characteristic frequency of each branch at the reference temperature expressed with the WLF law identified with experimental results and described in equation (5).

3.4 Identification methodology

With the virtual DMA experiments, in each direction $x \in (E, T, L, S1, S2)$, we find the storage and loss moduli of the projection as described in Equation (34). This parameters as shown in Fig.11 are related for each master curve obtained in each direction respectively to : i) the central characteristic frequency $M_x = log(f_x^{peak})$; ii) the wideness of the loss modulus peak approximately $\mathit{\Gamma}_x$; iii) the limits of the storage modulus when frequency tends to zero V_x^{ne} and finally; iv) the storage modulus when frequency tends to infinity $V_{x,ve}^{ne}$. For instance, in the case of the projection $P_{V_E}^{ne}$, the parameters will be M_α, $\mathit{\Gamma}_\alpha$, $V_{V_E}^{ne}$ and $V_{V_E,ve}^{ne}$. In the 3D spectral model, when the frequency tends to zero, the viscoelastic tensor $\boldsymbol{L}_{ve}^{V**}$ also tends

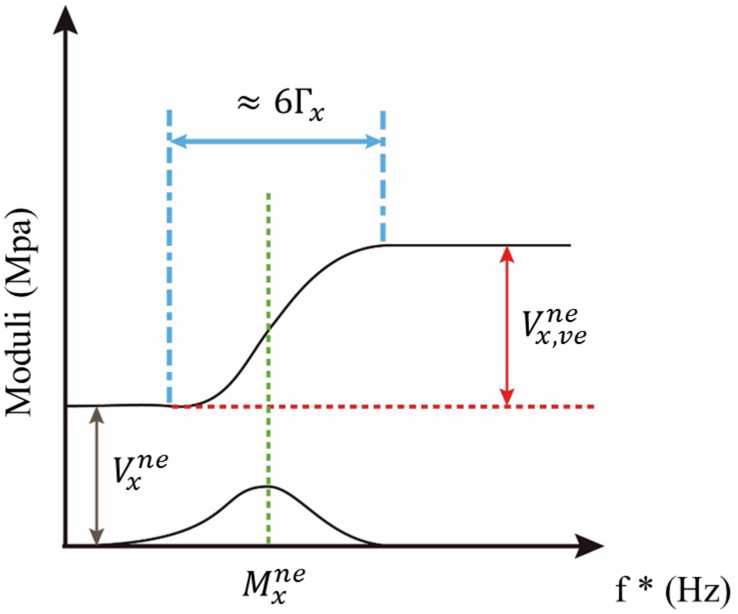

Fig. 11 Schematic layout of the identification methodology based on P_x^{ne} projection of numerical DMA results.

to zero as its behavior becomes more and more fluid like. Therefore, the only remaining stiffness contribution at very low frequency is $\boldsymbol{L}_{ve}^{E**}$. In the same way, when f^* tends to the infinity $\boldsymbol{L}_{ve}^{V**}$ tends to a finite value as the spring contributes more and more to the stiffness. The numerical values identified on virtual DMA master curves V_x^{ne} and $V_{x,ve}^{ne}$ can be used to identify the model parameters with the relation detailed in the equations (36), (37) and (38).

These nice relations allow to determine directly α_0, β_0 and λ_0 by calculating the limit of the $P_{V_{S1}}$, $P_{V_{S2}}$) and P_{V_E} projections when f^* tends to zero, and so that, in solving the following system:

$$\begin{cases} \lim\limits_{f^* \to 0} P_{V_{S1}} = & \frac{1}{2}(2\beta_0 + \sqrt{2}\lambda_0) & = V_{V_{S1}}^{ne} \\ \lim\limits_{f^* \to 0} P_{V_{S2}} = & \alpha_0 + \sqrt{2}\lambda_0 & = V_{V_{S2}}^{ne} \\ \lim\limits_{f^* \to 0} P_{V_E} = & \frac{2}{3}\alpha_0 + \frac{1}{2}\beta_0 - \frac{2\sqrt{2}}{3}\lambda_0 & = V_{V_E}^{ne} \end{cases}, \tag{36}$$

Similarly, δ_0 and γ_0 comes directly from the limit when f^* tends to zero of the P_{V_T} and P_{V_L} projections:

$$\begin{cases} \lim\limits_{f^* \to 0} P_{V_T} = \delta_0 = V_{V_T}^{ne} \\ \lim\limits_{f^* \to 0} P_{V_L} = \gamma_0 = V_{V_L}^{ne} \end{cases}. \tag{37}$$

Therefore $\alpha_{ve,0}, \delta_{ve,0}$ and $\gamma_{ve,0}$ are determined through the limit to the infinity of the $P_{V_E}(L_{ve}^{**})$, $P_{V_T}(L_{ve}^{**})$ and $P_{V_L}(L_{ve}^{**})$ projections:

$$\begin{cases} \lim\limits_{f^* \to \infty} P_{V_E} = & \frac{3}{2}\alpha_{ve,0} + \frac{2}{3}\alpha_0 + \frac{1}{2}\beta_0 - \frac{2\sqrt{2}}{3}\lambda_0 & = V_{V_E,ve}^{ne} \\ \lim\limits_{f^* \to \infty} P_{V_T} = & \delta_{ve,0} + \delta_0 & = V_{V_T,ve}^{ne} \\ \lim\limits_{f^* \to \infty} P_{V_L} = & \gamma_{ve,0} + \gamma_0 & = V_{V_L,ve}^{ne} \end{cases}. \tag{38}$$

The parameters Γ_x seem to be mostly matrix dependent. The parameter Γ_x defining the speed of the transition as related in Fig.9. Indeed, the identified values (fitted by trial and error) does not vary with either the fiber volume ratio, or the orientation distribution. Hence, for the rest of this work, we have chosen:

$$\Gamma_\alpha = \Gamma_\delta = \Gamma_\gamma = 6.1\ log(Hz). \tag{39}$$

The three remaining variables (M_α, M_δ and finally M_γ) are determined with the "Non-Linear Model Fit" function of Mathematica in using the virtual DMA curves and the P_{V_x} projections.

Thanks to this methodology, it is possible to accurately fit a 3D spectral model over experimental or virtual data. Fig.12 shows an example of fitted curves, for the P_{V_E} projection case, at different fiber volume fractions (5%, 15% and 25%).

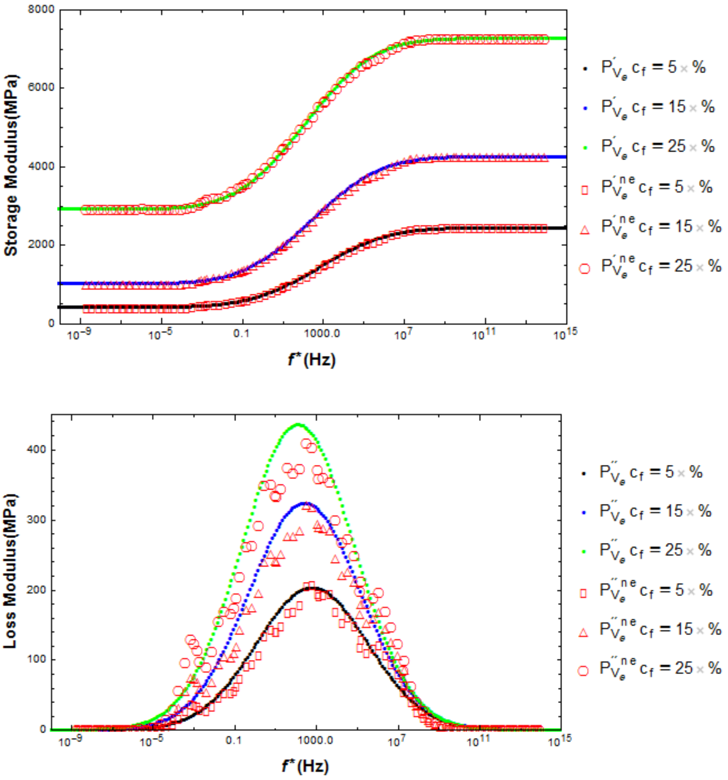

Fig. 12 3D spectral model fitted for the P_{V_E} projection CraFT generated DMAs, for 5%, 15% and 25% fiber volume ratio.

Using a spectral model is a good way to capture the glass fiber reinforced PEEK behavior. It shows a very good matching with CraFT data and also has the nice property of being defined by less material parameters than a generalized Maxwell model. This is encouraging in order to build a meta model, since the variable evolution will be easier to understand, and, in this case, we have uniqueness of the solution.

3.5 Fiber orientation characterization

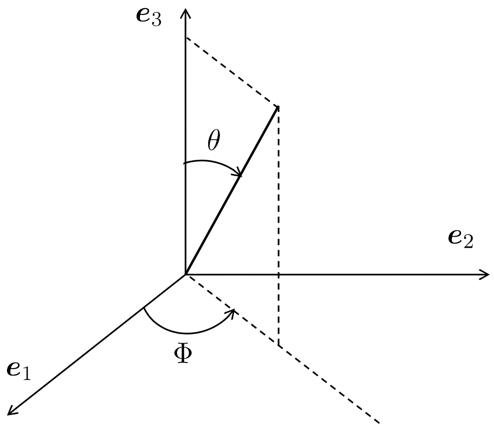

Fig. 13 Representation of the orientation vector of a single fiber [5].

When short fiber composite materials are processed through injection, the fibers in the matrix are mixed and disoriented. This results in variations in the orientation distributions depending on the position in the injected part. As a consequence, we need to measure and characterize this disorientation. Authors usually use orientation tensors to describe the microstructure [4, 5, 32]. Orientation tensors are defined at every even order by equations (40) and (41) in which a_2 and a_4 are respectively the second and fourth order definition of orientation tensors.

$$a_2 = \oint (O_v \otimes O_v)\psi(\theta, \Phi)dP, \tag{40}$$

$$a_4 = \oint (O_v \otimes O_v \otimes O_v \otimes O_v)\psi(\theta, \Phi)dP, \tag{41}$$

and O_v is the orientation vector of a single fiber, defined in the laboratory frame $(\overrightarrow{e_1}, \overrightarrow{e_2}, \overrightarrow{e_3})$ as (see as well Fig.13):

$$O_v = \begin{pmatrix} \sin\theta\cos\Phi \\ \sin\theta\sin\Phi \\ \cos\theta \end{pmatrix}_{(\overrightarrow{e_1}, \overrightarrow{e_2}, \overrightarrow{e_3})} \tag{42}$$

We need to use an accurate function $\psi(\theta, \Phi)$ to have a good representation of the reality. In the case of an orthotropic material such a distribution function can be written in the form [4]:

$$\psi(\theta, \Phi, N, Z) = \frac{\sin\theta^Z \cos\Phi^N}{\oint \sin\theta^Z \cos\Phi^N} \tag{43}$$

Varying N or Z will change the orientation distribution. The bigger N is, the more aligned along $\Phi = 0$ rad the fibers are. Similarly, the bigger Z is, the more aligned along $\theta = 0$ the fiber are. For this work, the material is assumed transverse isotropic. This assumptions allows a simplification of the density of probability function by taking $Z = N$ as:

$$\psi(\theta, \Phi, N) = \frac{\sin\theta^N \cos\Phi^N}{\oint \sin\theta^N \cos\Phi^N} \tag{44}$$

$N = 2$ implies that 60% of the fibers are aligned in the main axis (which is $\overrightarrow{e_1}$), the 40% remaining being distributed on the two other axes. $N = 60$ is considered as a quasi perfectly aligned fiber network, considering that 96.8% are perfectly aligned with the main axis. Fig.14 shows the probability density plotted for $N = 2$, $N = 8$ and $N = 60$, their associated second order orientation tensors and their Random RVEs (Representative Volume Elements) generated. These RVEs, while being more or less dispersed in terms of fiber orientation remains transversely isotropic.

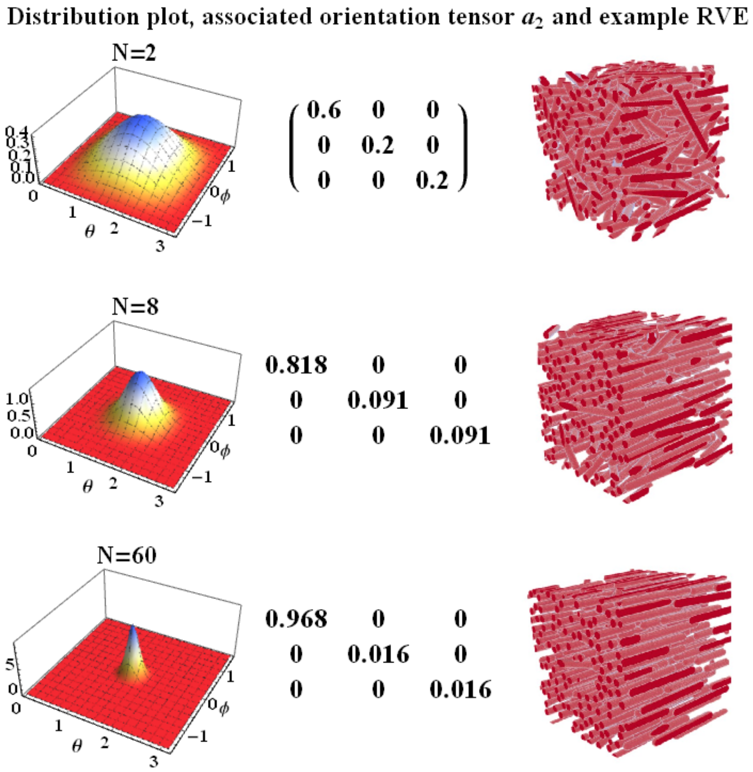

Fig. 14 Probability density plot, for $N = 0$, $N = 2$ and $N = 60$, along with the second order orientation tensors.

4 Meta-model

4.1 Definition

A meta model is a model that focuses on observing and predicting the evolution of the different variables of an initial model. In the present case, the objective is to observe the evolution of α_0, β_0, λ_0, δ_0, γ_0, $\alpha_{ve,0}$, $\delta_{ve,0}$, $\gamma_{ve,0}$, M_α, M_δ and finally M_γ . These 11 variables constitutes the whole 3D spectral model defined in section 3.2. The evolution of this group of variables is studied by varying the fiber volume ratio c_f, and the distribution of orientations characterized by N. $\mathit{\Gamma}$ remains constant in every direction and for every case. It is therefore not taken into account in the meta-modeling and remains constant as $\mathit{\Gamma} = 6.1 \; log(Hz)$. Each parameter needs to be fitted with a function, over the different variations. These variations were fitted in two steps: first, a mathematical function is used to fit the moduli changes over N. Figure 15 describes this step for the α_0 fit. While N grows, it follows an horizontal asymptotic trend (The exact limit depending on the fiber volume ratio). Indeed, the modulus for $N = 8$ is really close to the one for $N = 60$. The function used for this case takes the form:

$$\alpha_0(N, c_f) = a(c_f) \left[1 - e^{-b(c_f)N + c(c_f)}\right], \tag{45}$$

in which a was directly chosen to be equal to the data point for $N = 60$, b and c were fitted with the "non linear model fit" function of Mathematica. Then, one needs to study the evolution as a function of the volume ratio of the variables used to fit the data. In the α_0 case, the chosen function parameters are a, b, and c. These three variables showed quasi-linear variations. So, linear functions were used to fit these points. Fig.16 shows, from left to right the fits of a, b, and c.

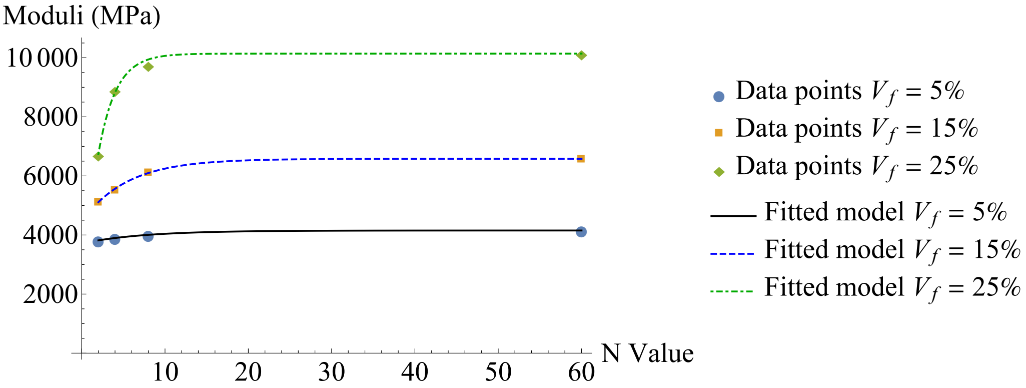

Fig. 15 Mathematical fit of the α_0 variation over N changes for three different volume ratios.

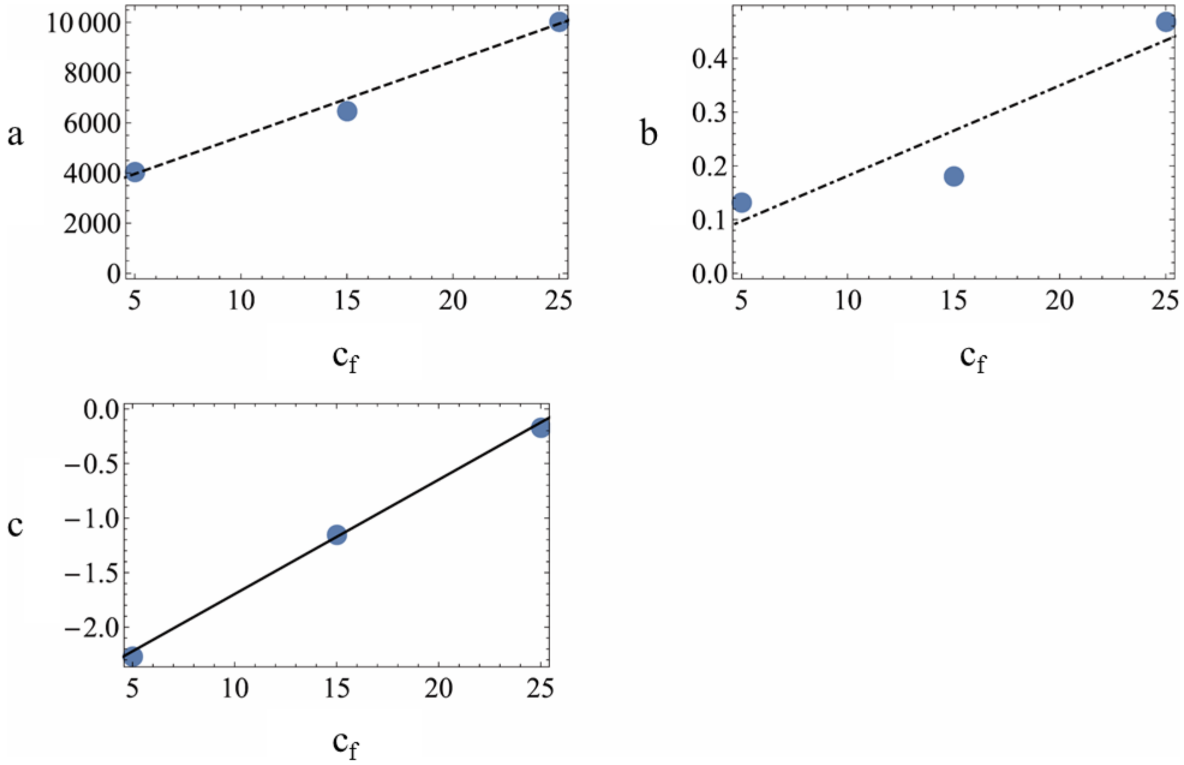

Fig. 16 Linear fit of the evolution of a, b, and c in the α_0 case.

Using this method, all the different variables were fitted as a function of N and c_f. The corresponding plot of the fit of all the other parameters can be found in the C.

4.2 Validation

The validation of the meta-model is done through a series of validation cases. To make sure that it matches the reality, a set of yet unused N and c_f values were taken: $N = 6$ and $c_f = 0.1$ or 0.2. For these, the meta-model-predicted storage and loss moduli are compared and for each loading case described in equation (30).

4.2.1 Check in the fiber direction: P_{V_E}

The $P^{'}_{V_E}$ and $P^{''}_{V_E}$ moduli is one of the most important parameters in the case of composite materials, because it is in the fiber axis. As N grows up, it is supposed to grow too since the bigger N is, the more fibers are aligned in this direction. The meta model gives a very good estimate for the $P^{'}_{V_E}$ and $P^{''}_{V_E}$ moduli and their evolution with frequency change, as shown in Fig. 17. It remains very close to the numerical experiment data and thus is very satisfying. The relaxation time, while not far from the matrix one, is also well captured.

4.2.2 Check in the first shear direction: P_{V_T}

The $P^{'}_{V_T}$ and $P^{''}_{V_T}$ moduli corresponds to the shear modulus in the plan perpendicular to the fibers (given by a V_T parallel DMA). On the contrary to the P_{V_E} complex moduli, the more N grows, the softer it becomes. Indeed, for a low N the fibers are more dispersed. This implies that more glass will have an active

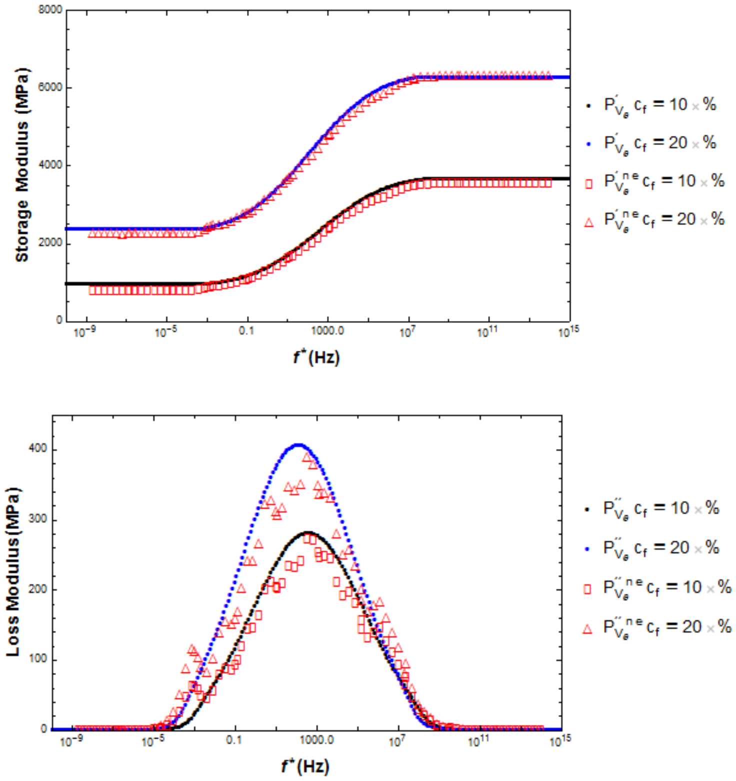

Fig. 17 Validation of the predicted P'_{V_E} and P''_{V_E} moduli for $N = 6$ and for $c_f = 10\%$ and $c_f = 20\%$.

role in the case of a shear loading, thus stiffening the modulus. Fig. 18 shows the meta-model estimation compared to the numerical experiment values. For this case, the meta model gives a very good estimation of the complex moduli, and their evolution with the frequency.

4.2.3 Check in the second shear direction: P_{V_L}

This second shear direction is the one given by V_L which corresponds to the two other shear directions. Fig. 19 shows the results. As P_{V_T} complex moduli, P_{V_L} complex moduli grow when N decreases. Except for the limit to infinity, where

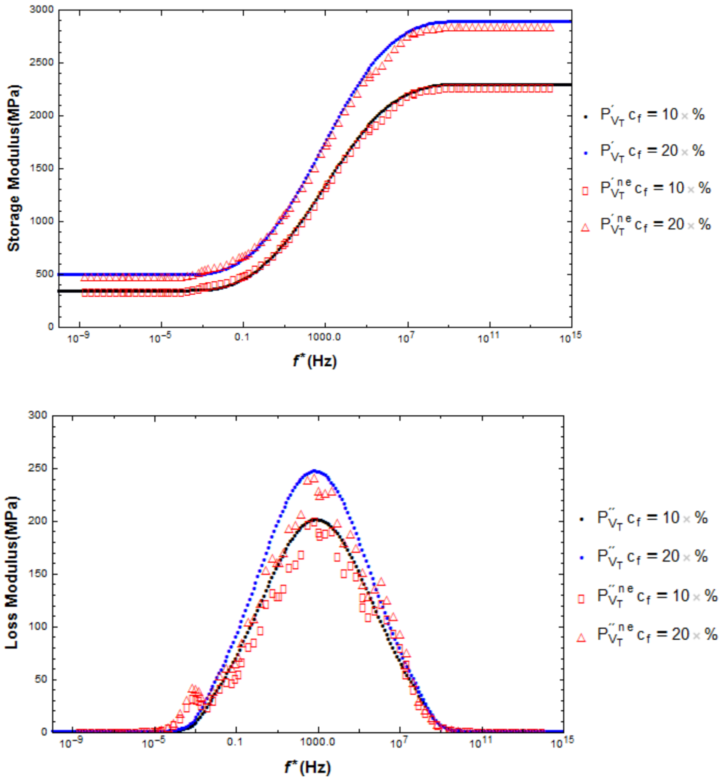

Fig. 18 Validation of the predicted P'_{V_T} and P''_{V_T} moduli for $N = 6$ and for $c_f = 10\%$ and $c_f = 20\%$.

the moduli are very slightly overestimated, the two curves are nearly perfectly superposed with their numerical experiment equivalent, which is very satisfying.

4.2.4 Check in the case of a perfectly spherical loading

While every moduli has been checked, the compressibility of the material made the model a bit more complex, this is why the parameters α_0, β_0, λ_0, δ_0 and γ_0 were introduced in equation (27). δ_0 and γ_0 are already validated by the low frequency fit in Figs. 19, and 18 (see equation (37)). But α_0, β_0, and λ_0 needs to be checked according to equation (36). For this, the RVEs are submitted to a DMA along V_S

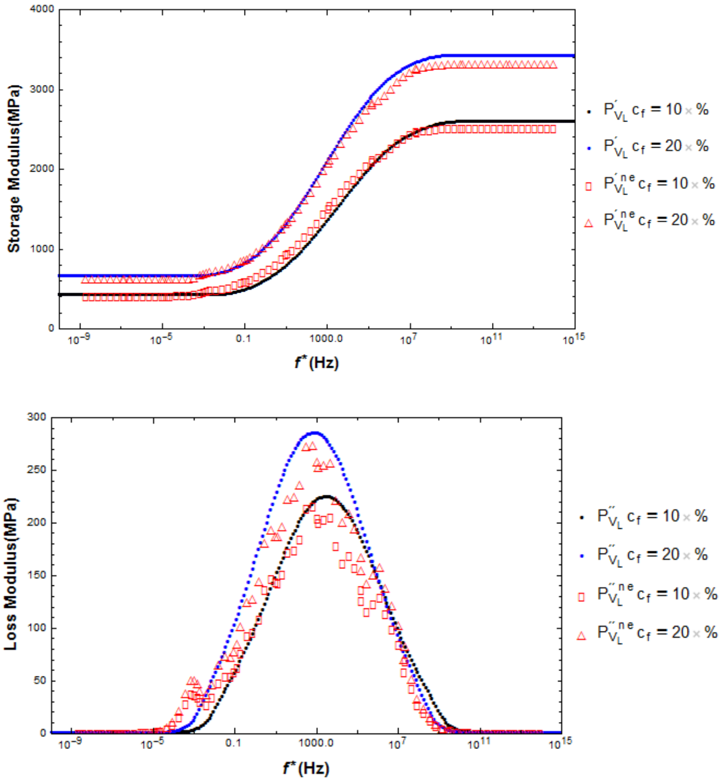

Fig. 19 Validation of the predicted P'_{V_L} and P''_{V_L} moduli for $N = 6$ and for $c_f = 10\%$ and $c_f = 20\%$.

(purely spheric loading), and the resulting stress and strains are then projected on the fiber axis $P_{V_{S1}}$ and the transverse axis $P_{V_{S2}}$ (see equations (30) and (31)).

$P_{V_{S1}}$ *projection*

The model has been built on the hypothesis that there is no dissipation on its spherical part. This was because the pure matrix behaves that way. Fig.20 shows the results of the $P_{V_{S1}}$ projection. The introduction of the fibers in the matrix seems to induce a dissipation phenomenon on pure spherical loadings. This phenomenon is unpredictable with the current form of the model. It thus creates an

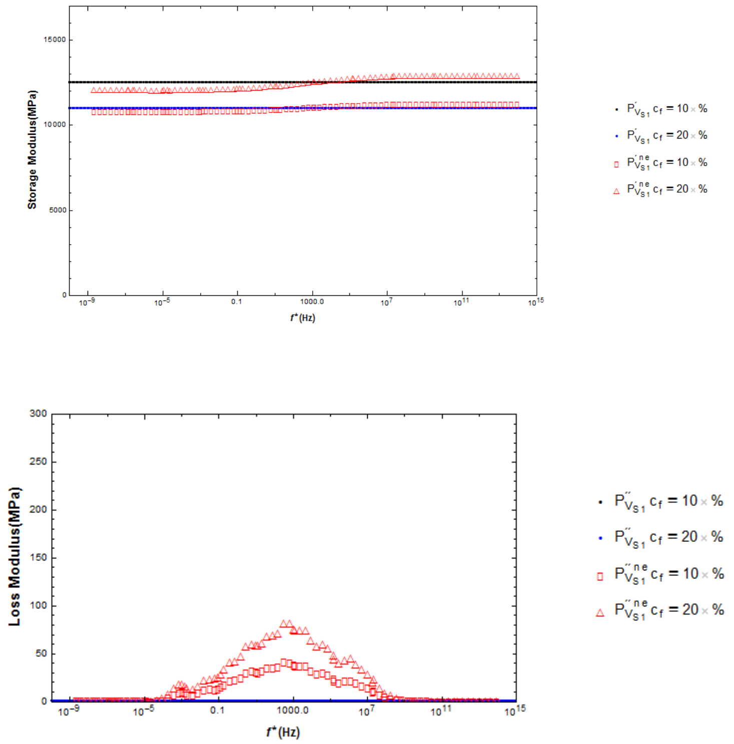

Fig. 20 Validation of the predicted $P_{V_{S1}}$ projection for $N = 6$ and for $c_f = 10\%$ and $c_f = 20\%$.

error between the real behavior and the model. The error is maximum at low frequencies and for $c_f = 20\%$ (and $N = 6$). But, at any point in the two test cases, it remains under 15% which seems to be acceptable.

$P_{V_{S2}}$ *projection*

The second projection is on the fiber axis. Dissipation phenomenon is also present, but at a much smaller scale. Fig. 21 displays the results of the $P_{V_{S2}}$ projection. The maximum error for this case is again for a 20% fiber volume ratio. As stated earlier, this error is much less than for the $P_{V_{S1}}$ projection. Indeed, it remains

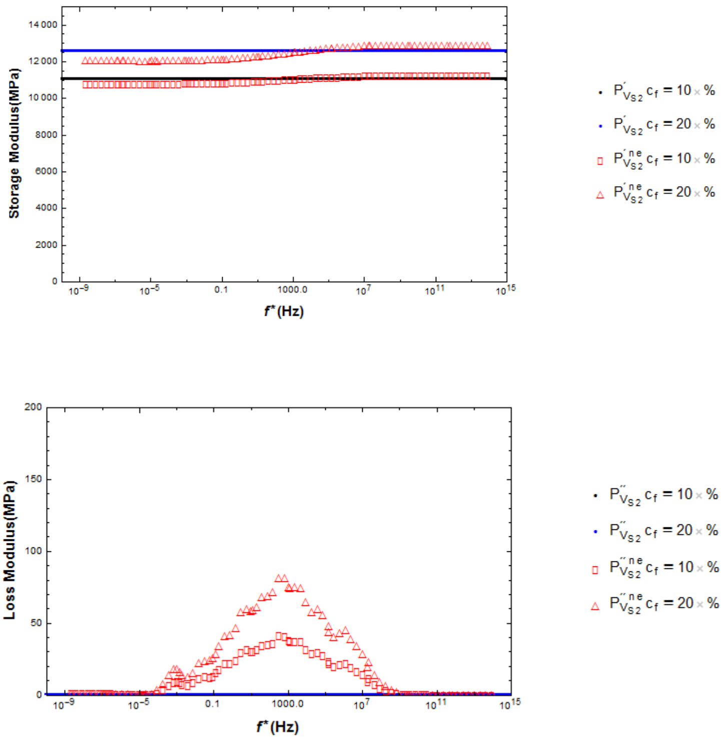

Fig. 21 Validation of the predicted $P_{V_{S2}}$ projection for $N = 6$ and for $c_f = 10\%$ and $c_f = 20\%$.

under 5.7% at any point. The predicted value seems to be a bit overestimated, but remains accurate.

4.3 Error between theoretical perfect fit and meta-model values

In order to make a last check on the meta-model validity, one can check the relative error between the meta model and the perfect fit values that would have been used should $N = 6$ and $c_f = 0.1$ or 0.2 be part of the model building cases. These values are gathered in Table 2. Thanks to those, one can say that the model gives an accurate prediction of the different material parameters. Indeed, the mean

Material Parameter	Relative Error (%) for $N = 6$	
	$c_f = 10\%$	$c_f = 20\%$
α_0	4.79	0.73
β_0	0.46	0.72
λ_0	0.51	1.48
δ_0	2.93	3.28
γ_0	1.42	5.54
$\alpha_{ve,0}$	2.00	3.77
$\delta_{ve,0}$	1.20	0.99
$\gamma_{ve,0}$	0.49	2.39
Mean error	1.73	2.36

Table 2 Table of all the relative errors obtained when comparing the best fit theoretical values with the ones given by the meta model (in %)

relative error in percent is of 1.73 % for the $c_f = 0.1$ validation case, and 2.36% when $c_f = 0.2$.

5 Conclusion

In this paper, we proposed a model for transversely isotropic and linear viscoelastic composite made of a PEEK matrix reinforced by short glass fibers. This model can take into account different fiber volume fraction and fiber orientation distribution which is characterized in this case by a single integer parameter. For each couple of microstructural parameters, viscoelastic law is found to fit some virtual DMA experiments obtained with full field calculations involving a Representative Volume Element characterized by the fiber volume fraction and the orientation distribution parameter and the fibers and matrix constitutive laws (linear elastic for the fibers and linear viscoelastic for the matrix). The macroscopic law is given by a spectral representation of a generalized Maxwell model. It is shown here that this representation allows to reduce drastically the number of material parameters which improve the identification procedure. Finally a meta-model is built by interpolating the material parameters of the macroscopic model for the studied set of fiber volume fraction and distribution orientation.

Comparisons with reference calculations show that this meta-model give very accurate estimate for the macroscopic linear viscoelastic behavior of such composites for all the microstructural parameters.

Future work improvements could be focused on the possible use of a more complex fiber orientation distribution to capture higher anisotropy degrees, for example,in the case of orthotropic materials, one could use the function given by equation (43) with different values of Z and N parameters.

The whole process of modeling was implemented with Python, C, CraFT and Mathematica following the framework displayed in Fig.22. All these steps could easily be wrapped up in a single software, for example for industrial applications.

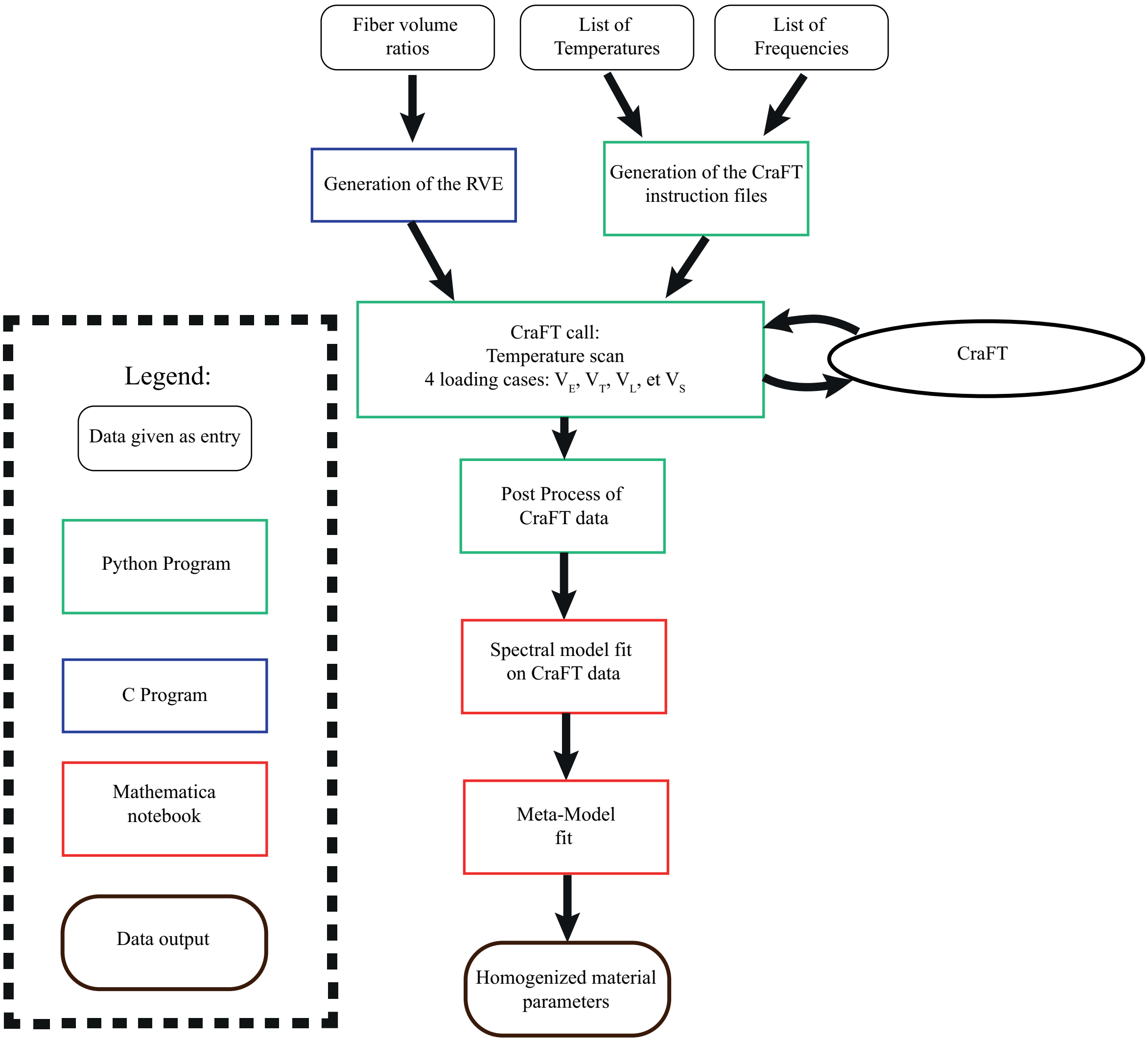

Fig. 22 Framework of the whole modeling process used in this PhD

Acknowledgements This project has received funding from the French Ministry of Higher Education and Research. We also want to thank PhD G.Robert in Solvay Company for supplying the PEEK composite material.

References

1. Solvay. KetaSpire PEEK design and processing Guide (2016)
2. D. Garcia-Gonzalez, M. Rodriguez-Millan, A. Rusinek, A. Arias, Composite Structures **133**, 1116 (2015). DOI 10.1016/j.compstruct.2015.08.028. URL `http://linkinghub.elsevier.com/retrieve/pii/S0263822315007059`
3. A. Chrysostomou, S. Hashemi, Journal of materials science **31**(5), 1183 (1996). URL `http://link.springer.com/article/10.1007/BF00353097`
4. S. Advani, C. Tucker, Journal of Rheology **31**, 751 (1987)
5. H. Shen, S. Nutt, D. Hull, Composites Science and Technology **64**(13-14), 2113 (2004). DOI 10.1016/j.compscitech.2004.03.003. URL `http://linkinghub.elsevier.com/retrieve/pii/S0266353804000612`
6. Friedrich, K, Walter, R, Voss, H, Karger-Kosis, J, Composites **17**(3), 205 (1986)
7. G.W. Milton, *The theory of composites* (Cambridge University Press, May 2002)
8. S. Kammoun, I. Doghri, L. Brassart, L. Delannay, Composites Part A: Applied Science and Manufacturing **73**, 166 (2015). DOI 10.1016/j.compositesa.2015.02.017. URL `http://linkinghub.elsevier.com/retrieve/pii/S1359835X1500069X`
9. N. Despringre, Y. Chemisky, K. Bonnay, F. Meraghni, Composite Structures **155**, 77 (2016). DOI 10.1016/j.compstruct.2016.06.075. URL `http://linkinghub.elsevier.com/retrieve/pii/S0263822316304238`
10. H. Moulinec, P. Suquet, Comptes rendus de l'Academie des sciences. Serie II, Mecanique, physique, chimie, astronomie **318**(11), 1417 (1994)
11. H. Moulinec, P. Suquet, Computer Methods in Applied Mechanics and Engineering **157**, 69 (1998)
12. J. Dirrenberger, S. Forest, D. Jeulin, International Journal of Solids and Structures **51**(2), 359 (2014). DOI 10.1016/j.ijsolstr.2013.10.011. URL `http://linkinghub.elsevier.com/retrieve/pii/S0020768313004009`

13. M. Lévesque, M.D. Gilchrist, N. Bouleau, K. Derrien, D. Baptiste, Computational Mechanics **40**(4), 771 (2007). DOI 10.1007/s00466-006-0138-6. URL `http://link.springer.com/10.1007/s00466-006-0138-6`
14. J.M. Ricaud, R. Masson, International Journal of Solids and Structures **46**(7-8), 1599 (2009). DOI 10.1016/j.ijsolstr.2008.12.007. URL `http://linkinghub.elsevier.com/retrieve/pii/S0020768308005027`
15. R. Masson, A. Zaoui, Journal of the Mechanics and Physics of Solids **47**(7), 1543 (1999). DOI 10.1016/S0022-5096(98)00106-9. URL `http://linkinghub.elsevier.com/retrieve/pii/S0022509698001069`
16. Y. Rougier, C. Stolz, A. Zaoui, Comptes rendus de l'Académie des sciences. Série II, Mécanique, physique, chimie, astronomie **316**(11), 1517 (1993)
17. N. Lahellec, P. Suquet, International Journal of Plasticity **42**, 1 (2013). DOI 10.1016/j.ijplas.2012.09.005. URL `http://linkinghub.elsevier.com/retrieve/pii/S0749641912001350`
18. L. Brassart, L. Stainier, I. Doghri, L. Delannay, International Journal of Plasticity **36**, 86 (2012). DOI 10.1016/j.ijplas.2012.03.010. URL `http://linkinghub.elsevier.com/retrieve/pii/S0749641912000502`
19. B. Burgarella, A. Maurel-Pantel, N. Lahellec, J.L. Bouvard, N. Billon, H. Moulinec, F. Lebon, Mechanics of Time-Dependent Materials pp. 1–24 (2018)
20. M.L. Williams, R.F. Landel, J.D. Ferry, Journal of the American Chemical Society **77**(14), 3701 (1955). DOI 10.1021/ja01619a008. URL `http://pubs.acs.org/doi/abs/10.1021/ja01619a008`
21. R. Li, Materials Science and Engineering: A **278**(1-2), 36 (2000). DOI 10.1016/S0921-5093(99)00602-4. URL `http://linkinghub.elsevier.com/retrieve/pii/S0921509399006024`
22. A. Maurel-Pantel, E. Baquet, J. Bikard, J. Bouvard, N. Billon, International Journal of Plasticity **67**, 102 (2015). DOI 10.1016/j.ijplas.2014.10.004. URL `http://linkinghub.elsevier.com/retrieve/pii/S0749641914001983`
23. R.D. Andrews, A.V. Tobolsky, Journal of Polymer Science **7**(23), 221 (1951). DOI 10.1002/pol.1951.120070210. URL `http://doi.wiley.com/10.1002/pol.1951.120070210`

24. J. Diani, P. Gilormini, C. Frédy, I. Rousseau, International Journal of Solids and Structures **49**(5), 793 (2012). DOI 10.1016/j.ijsolstr.2011.11.019. URL `http://linkinghub.elsevier.com/retrieve/pii/S002076831100401X`
25. D. Jalocha, A. Constantinescu, R. Neviere, International Journal of Solids and Structures **67**, 169 (2015)
26. B. Vieille, W. Albouy, L. Taleb, Composites Part B: Engineering **90**, 278 (2016)
27. W. Albouy, B. Vieille, L. Taleb, Composites Part A: Applied Science and Manufacturing **49**, 165 (2013)
28. A. Courtois, L. Marcin, M. Benavente, E. Ruiz, M. Lévesque, International Journal of Solids and Structures (2018). DOI https://doi.org/10.1016/j.ijsolstr.2018.12.018. URL `http://www.sciencedirect.com/science/article/pii/S0020768318305079`
29. H. Moulinec. Craft user guide (2014)
30. Craft (composite response and fourier transforms) a program to compute the mechanical response of heteregeneous materials. (Accessed 03.06.20]). URL `http://craft.lma.cnrs-mrs.fr/`
31. S. Staub, H. Andrä, M. Kabel, International Journal of Solids and Structures (2016)
32. I. Doghri, L. Tinel, International Journal of Plasticity **21**(10), 1919 (2005). DOI 10.1016/j.ijplas.2004.09.003. URL `http://linkinghub.elsevier.com/retrieve/pii/S0749641904001706`
33. M. Bornert, T. Bretheau, P. Gilormini, *Homogénéisation en mécanique des matériaux* (Hermès science publications, Paris, 2001)

A Maxwell model constants of the PEEK raw matrix

Parameters	Values
k	724.5
μ^1	206.2
η^1	10^{18}
μ^2	25.5
η^2	36000
μ^3	31.0219
η^3	1280
μ^4	50
η^4	130
μ^5	82.8
η^5	18
μ^6	90.9
η^6	2
μ^7	130.3
η^7	0.3
μ^8	123
η^8	0.032
μ^9	111.3
η^9	$2.5\ 10^{-3}$
μ^{10}	85.8
η^{10}	$1.2\ 10^{-4}$
μ^{11}	54.7
η^{11}	10^{-5}
μ^{12}	8.4
η^{12}	10^{-7}

Table 3 Maxwell model constants (MPa for μ^i and k, and in $MPa.s$ for η^i).

B transversely isotropic 4^{th} order tensor

In this appendix we give the expression of 4^{th} order tensors which are transversely isotropic with respect of one axis oriented by the vector n. It can be seen in [33] that every 4^{th} order tensor $\boldsymbol{A}$ transversely isotropic with major symetry can be written:

$$\boldsymbol{A} = \alpha \boldsymbol{E}_L + \beta \boldsymbol{J}_T + \lambda(\boldsymbol{F} + \boldsymbol{F}^T) + \delta \boldsymbol{K}_T + \gamma \boldsymbol{K}_L. \tag{46}$$

with :

$$\begin{aligned}
\boldsymbol{E}_L &= n \otimes n \otimes n \otimes n, \\
\boldsymbol{i}_T &= \boldsymbol{i} - n \otimes n, \\
\boldsymbol{J}_T &= \tfrac{1}{2} \boldsymbol{i}_T \otimes \boldsymbol{i}_T, \\
\boldsymbol{J} &= \tfrac{1}{3} \boldsymbol{i} \otimes \boldsymbol{i}, \\
\boldsymbol{F} &= \tfrac{\sqrt{2}}{2}(\boldsymbol{i}_T \otimes n \otimes n), \\
\boldsymbol{K} &= \boldsymbol{I} - \boldsymbol{J}, \\
\boldsymbol{K}_T &= \boldsymbol{I}_T - \boldsymbol{J}_T, \\
\boldsymbol{K}_E &= \tfrac{1}{6}\left(2n \otimes n - \boldsymbol{i}_T\right) \otimes \left(2n \otimes n - \boldsymbol{i}_T\right), \\
\boldsymbol{K}_L &= \boldsymbol{K} - \boldsymbol{K}_T - \boldsymbol{K}_E
\end{aligned} \tag{47}$$

In the case for which $\boldsymbol{A}$ project on the incompressible 2^{nd} order (i.e $\forall a \ tr(\boldsymbol{A} : a) = 0$). Then the expression 46 can be simplify by:

$$\boldsymbol{A} = \frac{3}{2} \alpha \boldsymbol{K}_E + \delta \boldsymbol{K}_T + \delta' \boldsymbol{K}_L. \tag{48}$$

with:

$$\boldsymbol{K}_E = \frac{2}{3} \boldsymbol{E}_L - \frac{\sqrt{2}}{3}(\boldsymbol{F} + \boldsymbol{F}^T) + \frac{1}{3} \boldsymbol{J}_T \tag{49}$$

when n is parallel to e_1 which the case studied in this paper, all the previous 4^{th} order tensor take the following expression:

$$\begin{aligned}
\boldsymbol{E}_L &= e_1 \otimes e_1 \otimes e_1 \otimes e_1, \\
\boldsymbol{J}_T &= \tfrac{1}{2}(e_2 \otimes e_2 \otimes e_2 \otimes e_2 + e_2 \otimes e_2 \otimes e_3 \otimes e_3 \\
&\quad + e_3 \otimes e_3 \otimes e_2 \otimes e_2 + e_3 \otimes e_3 \otimes e_3 \otimes e_3), \\
(\boldsymbol{F} + \boldsymbol{F}^T) &= \tfrac{1}{\sqrt{2}}(e_1 \otimes e_1 \otimes e_2 \otimes e_2 + e_1 \otimes e_1 \otimes e_3 \otimes e_3 \\
&\quad + e_2 \otimes e_2 \otimes e_1 \otimes e_1 + e_3 \otimes e_3 \otimes e_1 \otimes e_1), \\
\boldsymbol{K}_T &= \tfrac{1}{2}(e_2 \otimes e_2 \otimes e_2 \otimes e_2 + e_3 \otimes e_3 \otimes e_3 \otimes e_3) - \tfrac{1}{2}(e_3 \otimes e_3 \otimes e_2 \otimes e_2 + e_2 \otimes e_2 \otimes e_3 \otimes e_3) \\
&\quad + (e_2 \otimes e_3 + \otimes e_3 \otimes e_2) \otimes (e_2 \otimes e_3 + \otimes e_3 \otimes e_2), \\
\boldsymbol{K}_L &= (e_3 \otimes e_1 + \otimes e_1 \otimes e_3) \otimes (e_3 \otimes e_1 + \otimes e_1 \otimes e_3) + (e_1 \otimes e_2 + \otimes e_2 \otimes e_1) \otimes (e_1 \otimes e_2 + \otimes e_3 \otimes e_1)
\end{aligned} \tag{50}$$

C Meta-model values

The values that we got from the best fit for the meta model are reported in the two tables bellow. Table 4 gathers the functions used for the first step (evolution over N) and Table 5 gathers the functions used for the second step and the value of their parameters

Parameters	Mathematical function
α_0	$a_1(1-e^{b_1x+c_1})$
β_0	$a_2(1+e^{b_2x+c_2})$
λ_0	a_3x+b_3
δ_0	$a_4(1+e^{-b_4x+c_4})$
γ_0	$a_5(1+e^{-b_5x+c_5})$
$\alpha_{0,ve}$	$a_6(1-e^{-b_6x+c_6})$
$\delta_{0,ve}$	$a_7(1+e^{-b_7x+c_7})$
$\gamma_{0,ve}$	a_8x+b_8
M_α	$a_9(1+e^{-b_9x+c_9})$
M_δ	$a_{10}(1-e^{-b_{10}x+c_{10}})$
M_γ	$a_{11}(1-e^{-b_{11}x+c_{11}})$

Table 4 Type of function used to interpolate the values of the different parameters of the meta-model

Parameter	Mathematical function
a_1	$2466.84 + 299.381x$
b_1	$0.0132217 + 0.0168113x$
c_1	$-2.74547 + 0.0104865x$
a_2	$6589.54 + 49.4054x + 1.09223x^2$
b_2	$0.214646 - 0.00753747x + 0.000539186x^2$
c_2	$-3.94708 + 0.125997x + 0.000865784x^2$
a_3	$4384.68 + 83.0828x+$
b_3	$0.678292 - 0.102462x$
a_4	$212.171 + 11.9236x$
b_4	$0.301577 - 0.0223137x$
c_4	$-2.4499 + 0.0833838x$
a_5	$243.226 + 11.5072x$
b_5	$0.0192968 + 0.00382448x$
c_5	$-2.45768 + 0.104188x$
a_6	$1517.22 + 160.403x + 0.0426096x^2$
b_6	$0.129201 - 0.000507827x + 0.0000844632x^2$
c_6	$-1.86704 + 0.0823769 - 0.00147715x^2$
a_7	$1491.61 + 42.1352x$
b_7	$0.226345 + 0.00419678x$
c_7	$-3.12641 + 0.0613746x$
a_8	$1556.35 + 48.3409x$
b_8	$-0.48657 - 0.19709x$
a_9	$793.598 - 61.2738x + 1.13504x^2$
b_9	$0.246085 - 0.00542953 + 0.000597388x^2$
c_9	$-0.881393 + 0.173926x - 0.00286226x^2$
a_{10}	$1142.3 - 16.5853x$
b_{10}	$0.297326 - 0.00210555x$
c_{10}	$-2.47111 + 0.0553319x$
a_{11}	$1154.98 - 15.4951x$
b_{11}	$6.6146e^{3.1025-513412x}$
c_{11}	$21.2737 - 1.01799x$

Table 5 Table of the functions used to interpolate the second layer of parameters of the meta-model. These functions are used to determine the parameters of the functions displayed in Table 4